

Annular Dump Diffuser and Deswirl System for Back-Pressure Control in Engine-Scale Transonic Annular Cascade

Mathias Michaud

Department of Engineering Science,
University of Oxford,
Parks Road,
Oxford OX1 3PJ, UK
e-mail: mathias.michaud@eng.ox.ac.uk

Francesco Ornano

Department of Engineering Science,
University of Oxford,
Parks Road,
Oxford OX1 3PJ, UK
e-mail: francescoguido.ornano@ingpec.eu

Thomas Povey¹

Department of Engineering Science,
University of Oxford,
Parks Road,
Oxford OX1 3PJ, UK
e-mail: thomas.povey@eng.ox.ac.uk

A common requirement for turbomachinery testing facilities is the ability to independently control Mach number and Reynolds number. In practice, this means independent control of the inlet total pressure and exit static pressure in a test facility. In this paper, we present a solution to this problem with particular applicability to large-scale annular test facilities. We describe the design and commissioning of a combined annular dump diffuser and deswirl system for back-pressure control in environments with high-whirl transonic flow. The particular application was an annular cascade of nozzle guide vanes from a current civil engine. The purpose was to provide independent control of Mach number and Reynolds number, by controlling the back-pressure in the intermediate annular plenum which forms the dump diffuser. The dump diffuser is necessary to facilitate optical and probe access (without interaction effects) and to reduce the risk of exit static pressure disturbances (due to particular duct design). The system has been installed and validated in the engine component aerothermal (ECAT) facility at the University of Oxford. In this implementation of the system, the high-whirl transonic flow from the nozzle guide vanes passes through a short, parallel annular duct, and is dumped into an annular plenum, before being re-accelerated into a deswirl vane ring. The deswirl ring turns the flow to the axial direction. The flow is then discharged through a variable choke plate into a silencer. Conditioning the flow to have zero whirl at the choke plate reduces the sensitivity of the choke plate effective blockage to the whirl angle. The design, deswirl vane aerodynamic performance, and overall system performance are assessed with detailed experiments and 3D unsteady computational fluid dynamics predictions. The control of high-whirl transonic flow is notoriously challenging, and the deswirl system has application to exhaust conditioning in a number of applications including annular cascade experiments and rocket turbo-pump exhaust systems. [DOI: 10.1115/1.4055863]

Keywords: computational fluid dynamics (CFD), fan, compressor, and turbine aerodynamic design, fluid dynamics and heat transfer phenomena in compressor and turbine components of gas turbine engines, measurement techniques, turbine blade and measurement advancements, turbomachinery blading design

Introduction and Related Literature

To fully match non-dimensional conditions relevant to aerodynamic and heat transfer testing of turbomachinery components, it is necessary to provide independent control of exit Mach number and Reynolds number. This is achieved by having independent control of the inlet total pressure and exit static pressure. Control of the inlet total pressure is normally via compressor control (in continuously running facilities) or a combination of regulators and limiters (in blowdown facilities). Most continuously running facilities control the exit static pressure using a vacuum pump [1–3], or a vacuum pump in combination with a throttle [4–7]. In blowdown facilities, control of the exit static pressure is normally achieved with an exit throttle, both for atmospheric-back-pressure [8–11] and evacuated-tank [12–16] facilities. In transonic blowdown linear cascades, simple valves and nozzles have been used for back-pressure control, typically integrated into the exit duct of the cascade [17,18]. In transonic blowdown annular cascades (both rotating and non-rotating), accurate back-pressure control with an

area-limiting device is complicated by the swirling motion of the flow. This is particularly true in high-pressure (HP) nozzle guide vane (NGV) cascades or 1.5 stage turbine configurations [19,20] in which there is a high exit swirl angle (typically above 70 deg). Back-pressure control in single stage turbine configurations is often relatively simpler because exit swirl angles are typically below 30 deg [8,12]. In cases with high exit swirl angle, traditional choke plates (slotted plate controlling the flow area when rotated around its axis, see for example, Refs. [12,13]) might be expected both to have extremely high minimum blockage—even in the fully open position—on account of gross separation from the individual radial elements and to have high sensitivity to the swirl angle. Thus, more sophisticated back-pressure control systems may be required. To overcome the problems associated with traditional choke plates, three alternative concepts have been deployed: the radial-flow sleeve throat [14], the annular second throat (an adjustable annular nozzle) [6,15,16 and discussion in 10], and the deswirl vane with choke plate combination [9–11,19,20, and present study]. Table 1 summarizes the major transonic annular turbine cascade facilities (continuous running and blowdown) and their back-pressure control systems.

We review the annular nozzle and deswirl vane concepts briefly. The adjustable annular nozzle is conceptually simple and—provided that the mean radius of the flow path is well matched—is unlikely to have unusual swirl sensitivity. A significant

¹Corresponding author.

Contributed by the International Gas Turbine Institute (IGTI) of ASME for publication in the JOURNAL OF TURBOMACHINERY. Manuscript received May 8, 2021; final manuscript received August 19, 2022; published online November 4, 2022. Assoc. Editor: Randall M. Mathison.

Table 1 List of the back-pressure control systems used in major transonic turbine annular cascades

Facility name	Cascade type	Institution	Back-pressure control system
Transonic Turbine Test Facility [1]	Rotating	TU Graz	Vacuum pump
High Speed Annular Cascade [2]	Annular	Cambridge	Vacuum pump
High Work Research Turbine [3]	Rotating	Pratt & Whitney Canada	Vacuum pump
Notre-Dame Turbomachinery Laboratory [4]	Rotating	Notre-Dame	Valve and vacuum pump
Annular Sector Cascade [5]	Annular sector	Royal Institute of Technology	Butterfly valve and vacuum pump
Oxford Rotor Facility [12]	Rotating	Oxford	Choke plate
CT3 [13]	Annular/rotating	von Karman Institute	Choke plate
Blowdown Turbine Facility [14]	Rotating	Massachusetts Institute of Technology	Sleeve throat
Turbine Test Facility [15]	Rotating	Ohio State	Annular nozzle
Purdue Experimental Turbine Aerothermal Laboratory [16]	Rotating	Purdue	Annular nozzle
Oxford Turbine Research Facility (OTRF) [8]	Rotating	Oxford	Annular nozzle
OTRF [10]	Rotating	Oxford	Deswirl and choke
Sector [11]	Annular sector	Oxford	Deswirl and choke
ECAT/ECAT + (present study)	Annular	Oxford	Deswirl and choke
NG-Turb [6]	Rotating	German Aerospace Center (DLR)	Vacuum pump and shutters
Rotating Cascade Tunnel in Göttingen [7]	Rotating	DLR	Vacuum pump and shutters

disadvantage, however, is the necessity of providing a support structure for the inner-radius parts of the system. In a turbine system with shaft support structure this may be easily accommodated (the downstream end of the turbine shaft is normally supported by a series of structural struts), but in a NGV cascade this requirement is likely to add significant complexity, weight, axial length, and cost.

The deswirl vane with choke plate combination works on the principle of first removing the swirl, then throttling the flow. This allows for low minimum blockage and low sensitivity of the choke plate to the swirl angle. Such systems have been deployed successfully in annular sector cascades [11] and fully annular cascades [19,20] and have been proven to provide excellent fine control of back-pressure. The disadvantage, of course, is the relative complexity of the aerodynamic design, and the fact that such systems have relatively high sensitivity to swirl angle *changes*: that is, the deswirl vane is optimized for a particular cascade exit angle. Previous systems have been designed with unseparated intermediate ducts (both annular sector [11] and fully annular [19,20]). Although this leads to the lowest total pressure loss (in principle, zero loss) connection between the cascade exit and the choke plate, and therefore allows for the most compact deswirl vane, there are two disadvantages: the further design requirement for the interconnecting duct and the residual problem of high *local* back-pressure sensitivity to blockage within the duct (from probes or cameras, for example). By employing a dump diffuser upstream of the deswirl vanes—unique to the present

system—the local back-pressure sensitivity to instrumentation is removed, allowing greater freedom for downstream traverse systems and camera instrumentation.

This first known implementation of a combined dump diffuser deswirl vane control system is presented in this paper. The system was installed and validated on the Engine Component AeroThermal (ECAT) facility at the University of Oxford, a transonic, fully annular, engine-scale HP NGV cascade. Detailed experimental measurements at a wide range of operational conditions are combined with 3D unsteady computational fluid dynamics (CFD) predictions to understand the performance of this new flow control system. The work is presented in the following order: overview of the facility, preliminary design, mechanical assembly, experimental methods, numerical methods, and results.

Overview of the Experimental Facility

The ECAT facility at the University of Oxford is a semi-transient fully annular cascade of real engine HP NGVs [21]. Figure 1 shows a cross-sectional schematic of the ECAT facility. The original facility is identified with solid hatching lines while the new deswirl module is identified with the dashed hatching lines. The measurement stations of the facility are identified in Fig. 1: (1) upstream of the HP NGVs, (2) downstream of the HP NGVs, (3) HP NGV exit duct outlet, (4) upstream of the deswirl vanes, and (5) downstream of the deswirl vanes (detuner). We will refer to these stations

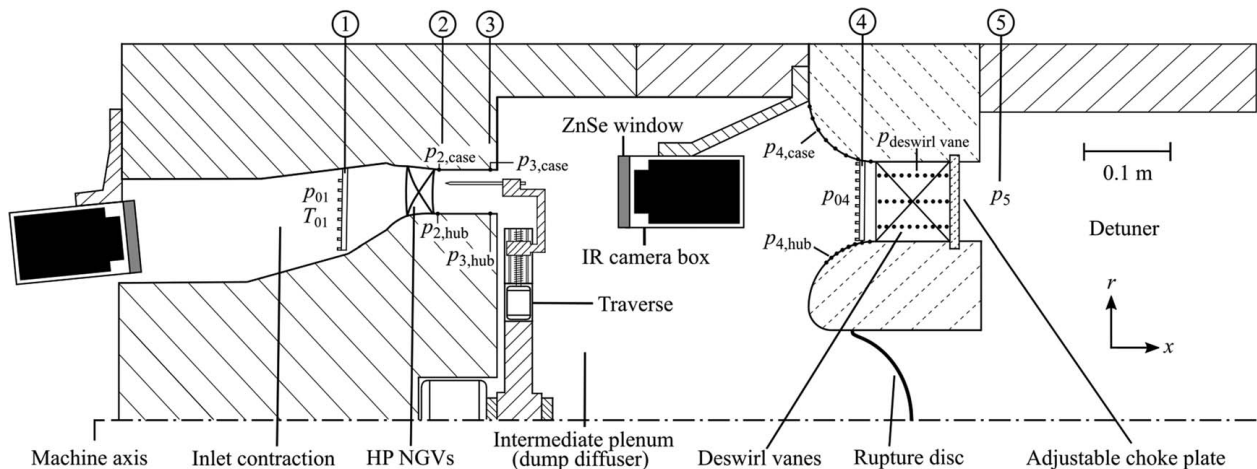


Fig. 1 Sectional schematic of the ECAT/ECAT + facility with the new deswirl module

Table 2 ECAT + facility operating conditions

Parameter	Cold	Warm	Hot
Extended inlet total pressure, p_{01} (bar)	1 – 6	1 – 6	1 – 6
Extended inlet total temperature, T_{01} (K)	285	345	600
Vane exit Mach number, M_2	0.70 – 1.21	0.70 – 1.21	0.70 – 1.21
Natural exit Reynolds number at $M_2 = 1$, Re_2	1.81×10^6	1.39×10^6	0.69×10^6
Extended <i>minimum</i> exit Reynolds number at $M_2 = 1$, $Re_{2,min}$	1.87×10^6	1.44×10^6	0.74×10^6
Extended <i>maximum</i> exit Reynolds number at $M_2 = 1$, $Re_{2,max}$	5.79×10^6	4.51×10^6	2.27×10^6

in later sections. During a test, the high-pressure air stored in large tanks is discharged through the cascade in regulated or blowdown mode (more details later). In the original facility (without back-pressure control), the air exits the NGVs and passes through a short parallel annular duct (to maintain pressure gradients similar to those in an engine) before being dumped into a large detuner at atmospheric conditions. The facility achieves a high degree of non-dimensional similarity to engine operating conditions by matching the NGV exit Mach number M_2 , NGV exit Reynolds number Re_2 (based on NGV true chord) near cruise and coolant-to-mainstream pressure ratio. Nominal operating conditions are given in Table 2.

The facility was developed for extremely accurate measurement of metal effectiveness [21], aerodynamic performance [21,22], and capacity [23–25]. Further details of the general capability can be found in Ref. [21]. To perform these measurements, it is necessary to have optical access from both upstream and downstream (infrared cameras and traverse probes), and a radial back-pressure condition typical of that in the engine situation.

The M_2 – Re_2 characteristic of the HP NGVs develops naturally, and it is fortuitous that at typical cold-rig and warm-rig operating conditions M_2 and Re_2 are simultaneously well matched to engine cruise conditions with atmospheric back-pressure. The facility is currently being upgraded for operation at engine realistic coolant-to-mainstream temperature ratios (known as the ECAT + facility) [26], a condition at which the natural Re_2 is less well matched. The *natural characteristics* (without the deswirl module installed) at typical cold-, warm-, and hot-rig conditions along with typical engine operating points (max-take-off, MTO, and cruise) are shown in Fig. 2 for the ECAT + facility.

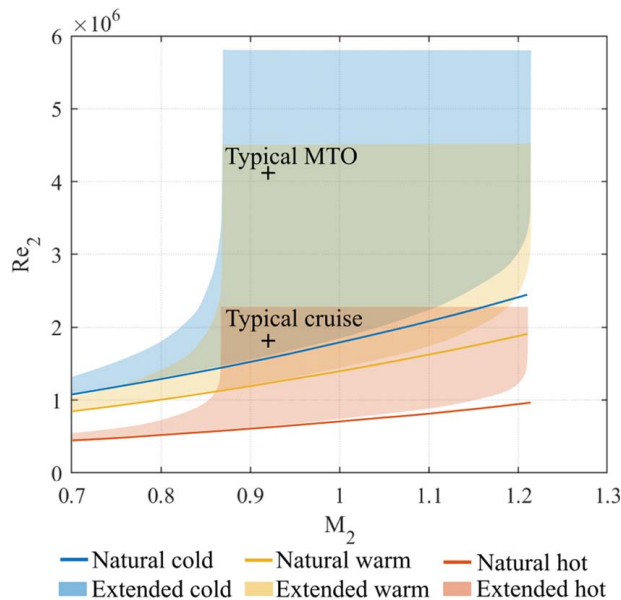


Fig. 2 Natural operating characteristics for the ECAT + facility in cold-, warm-, and hot-rig operation; extended operating range with deswirl module; engine cruise and MTO conditions

The purpose of the dump diffuser and deswirl system is to extend the operating range of the facility to higher Re_2 (at a given M_2), by means of back-pressure control, without limiting instrumentation access to the facility (optical and traverse). The maximum operating total pressure upstream of the NGVs (p_{01}) is 6 bar [26]. The maximum operating temperature (T_{01}) with extended temperature range is 600 K [26]. With the operating envelope in pressure and temperature defined for the ECAT + facility (Table 2), the M_2 – Re_2 operating space with the deswirl module at cold-, warm-, and hot-rig operating conditions are delimited by the shaded area in Fig. 2.

Back-Pressure Control System Design

In this section, we describe the design of the back-pressure control system for the ECAT and ECAT + facilities. The purpose is to provide independent control of the NGV cascade Reynolds and Mach numbers.

The general concept is shown in sectional view in Fig. 1. Downstream of the test NGV cascade (the ECAT or ECAT + module), there is a dump diffuser followed by a ring of deswirl vanes with a downstream adjustable choke plate. The NGV cascade is typically operated in the transonic regime with high exit whirl angle (typically $\beta_2 > 70$ deg). To reduce the chance of separation of the hub boundary layer at the vane exit plane and to provide an axial region for downstream traversing, the flow first passes through a parallel duct (typically 2–2.5 axial chords in length) before being dumped into the intermediate annular plenum (the dump diffuser). The flow is then re-accelerated through an inlet contraction into a deswirl vane ring. The deswirl vanes turn the flow to the axial direction and the flow is then discharged through a variable choke plate into a detuner at atmospheric pressure. The dump diffuser allows significant freedom for a downstream traverse system and infrared cameras.

We now consider the following topics in more detail: deswirl vane conceptual design, preliminary aerodynamic design and capacity setting, deswirl vane count, the mechanical design, and the choke plate design.

Deswirl Vane Conceptual Design. A schematic of the deswirl vane concept is shown in Fig. 3(b). The concept is an impulse-type transonic turbine blade (Fig. 3(a)) truncated at half chord, where the flow direction is approximately axial. The leading edge (LE) is relatively sharp (circular arc of 0.5 mm radius) to avoid detached shocks in mildly supersonic regions. The passage is of constant area design to turn the flow without diffusion, thus reducing the chance of boundary layer separation and associated blockage. Deswirl vanes of similar design have been successfully used for high-whirl transonic flow control in fully annular cascades of intermediate-pressure nozzle guide vanes [19,20,10], annular sectors of HP NGVs [11,27], and also in rocket turbo-pump exhaust systems.

Preliminary Aerodynamic Design and Capacity Setting. The mean metal angle of the LE of the deswirl vanes was chosen to have a small nominal positive incidence angle. The logic is that a separation bubble on the uncovered suction surface (SS) surface is likely

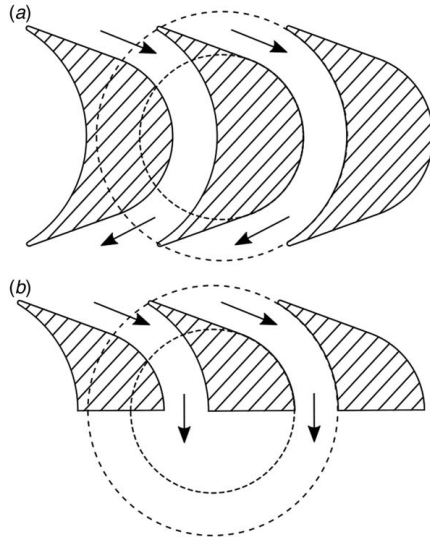


Fig. 3 (a) Impulse turbine blade design and (b) impulse-type deswirl vane based on Ref. [10]

to collapse before the flow enters the covered passage, leading to relatively low blockage and loss, but a separation bubble on the pressure surface (PS) would more directly impact the vane aerodynamics. For the first implementation of the system (a typical ECAT HP NGV test module), the mass-flux-averaged exit yaw angle measured from the HP NGVs in a previous experimental campaign [22] was $\beta_2 = 75.8$ deg. The exit yaw angle is measured from the axial direction. The corresponding CFD-predicted mass-flux-averaged yaw angle at the deswirl vane inlet plane was 77.0 deg (Fig. 4). The deswirl vane nominal LE metal angle before the LE radius was applied was 74.0 deg leading to a nominal incidence angle (for area-ratio calculations) of 3.0 deg based on the CFD-evaluated angle, or a capacity increase based on area (for a given span) of 14%. This reduces the required span of the deswirl vane necessary to maintain an adequate *capacity overhead*: that is, sufficiently larger area that even accounting for all total pressure loss between the NGV exit and deswirl vane inlet a low minimum back-pressure can be achieved with the system installed. The LE cutback decreases the PS metal angle to 70.0 deg, leading to a nominal predicted PS incidence angle of 7.0 deg (SS metal angle is unchanged at 74.0 deg; see Fig. 4).

The deswirl vane mean radius was chosen to be similar to that of the NGV (360 mm versus 371 mm), but the span was increased (100 mm compared to 53 mm for the NGV) to allow sufficient capacity overhead (with respect to the HP NGV flow capacity). We define the HP NGV flow capacity

$$\Gamma_1 = \frac{\dot{m}\sqrt{T_{01}}}{p_{01}} \quad (1)$$

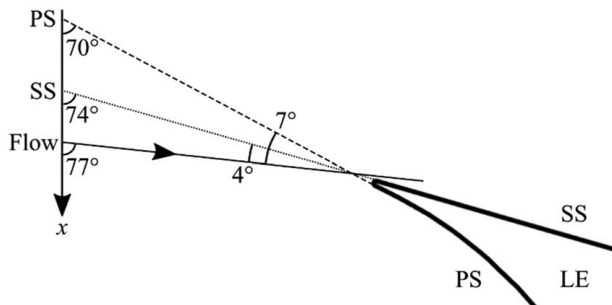


Fig. 4 Nominal incidence angles at the LE of the deswirl vane

where \dot{m} is the mass flowrate, and p_{01} and T_{01} are the total pressure and total temperature—respectively—measured upstream of the HP NGVs (see Fig. 1). We can also define the isentropic geometric capacity function [25] of the deswirl vanes $\Gamma_{4, is}$ based on the geometric passage area $A_{4, g}$:

$$\Gamma_{4, is} = A_{4, g} \sqrt{\frac{\gamma}{R} \left(\frac{p_5}{p_{04}} \right)^{(\gamma+1)/2\gamma}} \left\{ \left[\left(\frac{p_5}{p_{04}} \right)^{(1-\gamma)/\gamma} - 1 \right] \frac{2}{\gamma-1} \right\}^{1/2} \quad (2)$$

where p_{04} is the deswirl vane upstream total pressure, and p_5 is the deswirl vane downstream static pressures (see Fig. 1). This gives an *ideal* deswirl-to-NGV capacity ratio $\Gamma_{4, is}/\Gamma_1 = 2.57$ at a Mach number of unity at the NGV exit. Assuming a deswirl vane capacity deficit ζ (effective blockage factor to account for secondary flow and loss *within* the deswirl vane passage) of 0.20, we estimate a *predicted* effective deswirl-to-NGV capacity ratio of $\Gamma_{4, predicted}/\Gamma_1 = 2.06$ (Mach number of unity at the NGV exit).

The value of $\zeta = 0.20$ for preliminary design was justified on that basis that it is twice the typical maximum effective blockage of carefully designed HP NGVs (typically $\zeta < 0.1$). This accounts for greater secondary flows and loss within the impulse-turbine-type passage.

We now define a mass-flux-averaged dump diffuser total pressure loss coefficient by

$$Y_{p, DD} = \frac{\bar{p}_{02} - \bar{p}_{04}}{\bar{p}_{02} - p_2} \quad (3)$$

where \bar{p}_{02} is the mass-flux-averaged total pressure downstream of the NGVs, p_2 is the static pressure downstream of the NGVs, and \bar{p}_{04} is the mass-flux-averaged total pressure upstream of the deswirl vanes. Regarding the preliminary value of $Y_{p, DD} = 0.5$, there is no literature (to the authors knowledge) reporting total pressure loss coefficient in a transonic annular dump diffusion. We therefore used a sudden expansion total pressure loss coefficient in a cylindrical pipe [28], taking the external diameter of the NGV exit duct as the small diameter and the diameter of the intermediate plenum as the large diameter.

For design, we take a value—from experiment [22]—of $Y_{p, NGV} = 0.05$.

$$Y_{p, NGV} = \frac{p_{01} - \bar{p}_{02}}{p_{01} - p_2} \quad (4)$$

We now specify the following nominal operating conditions for the zero blockage at the deswirl vane exit plane: atmospheric pressure ($p_5 = 1$ bar); a Mach number of unity at the NGV exit ($M_2 = 1$ or $p_{01}/p_2 = 1.89$); $\Gamma_{4, predicted}/\Gamma_1 = 2.06$; $Y_{p, DD} = 0.5$; $Y_{p, NGV} = 0.05$. Using these values with *locally* (NGV row or deswirl row in isolation) isentropic capacity characteristics, we can back-calculate the following: deswirl vane inlet total pressure, p_{04} ; intermediate plenum static pressure, p_2 ; NGV downstream and upstream total pressures, p_{02} and p_{01} , respectively; and NGV Reynolds number, Re_2 . The resulting values are summarized in Table 3. Greater assumed values of $Y_{p, DD}$ and ζ would lead to a larger required deswirl vane span (increased flow capacity) to maintain the same minimum NGV back-pressure. Making such an assumption would be more conservative in terms of flow capacity overhead, but would lead to a larger system with greater manufacture cost.

Under cold conditions, the minimum NGV Reynolds number with the system installed was $Re_2 = 1.87 \times 10^6$, 3.32% higher than without a back-pressure control system ($Re_2 = 1.81 \times 10^6$). The conclusion based on the preliminary design values is that the capacity overhead is sufficient to provide flexibility for low-Re conditions. The maximum Re_2 is determined either by the design pressure capability of the upstream vessel (10 bar for ECAT and 15 bar for ECAT+) or the maximum mass flowrate with the current metering system (equivalent to upstream total pressure of 4.0 bar for ECAT and 6.0 bar for ECAT+, for typical NGV capacity).

Table 3 Preliminary design input and output parameters with zero choke plate blockage ratio

Preliminary design input parameter	NGV	Deswirl
Midspan radius (mm)	371	360
Span (mm)	53	100
Ideal capacity ratio, $\Gamma_{4,ideal}/\Gamma_1$	2.57	
Assumed deswirl vane capacity deficit, ζ	0.20	
Predicted capacity ratio, $\Gamma_{4,predicted}/\Gamma_1$	2.06	
Dump diffuser loss coefficient, $Y_{p,DD}$	0.50	
NGV loss coefficient, $Y_{p,NGV}$	0.05	
NGV exit Mach number, M_2	1.00	
System back-pressure, p_5 (bar)	1.00	
Preliminary design output parameter		
Deswirl vane inlet total pressure, p_{04} (bar)	1.47	
Intermediate plenum static pressure, p_2 (bar)	1.03	
NGV exit total pressure, p_{02} (bar)	1.90	
NGV upstream total pressure, p_{01} (bar)	1.95	
Minimum Re_2 with deswirl system	1.87×10^6	
Reference values without deswirl system		
Minimum Re_2 without deswirl system	1.81×10^6	
Increase in minimum Re_2 with deswirl (%)	3.32	

For the NGV ring used in this study (which is typical of large civil engines), the increase in Re_2 above the minimum value to match the cruise and MTO operating points at $M_2=0.92$ (see Fig. 2) were 15.3% and 162%, respectively. At cold-ECAT conditions, upstream total pressures of 1.95 bar and 4.41 bar—respectively—are necessary. Using the prelim-design method, this is equivalent to choke plate blockage factors of 0.30 and 0.37, respectively. To provide additional headroom, the maximum choke plate blockage factor was set to 0.50. At this value, the predicted total pressure upstream of the NGV is $p_{01}=5.85$ bar, well below the design pressure (10 bar).

Deswirl Vane Count. For a given deswirl vane midspan radius, span, and specified metal angle, the capacity ratio is unaffected by the vane count. The axial chord of the deswirl vane is proportional to vane count, however. Lower vane count therefore implies: stiffer vanes (important if the vane is to be used structurally as a blisk), lower total pressure loss (same wetted surface area, but reduced

average shear), higher weight (approximately inversely proportional to vane count), and longer range LE potential field interaction. A vane count of 30 was chosen, which is a compromise between these competing design requirements. For NGV rings with 40 vanes (typical installation), this gives a beat count (peak count in interference pattern) of 10, suggesting low potential field interaction effects at the NGV exit plane.

Mechanical Design. Figure 5 shows the front and back views of the deswirl module. The deswirl vane ring was machined as a blisk, providing structural support for the hub components and rupture disc. The blisk was machined from 17–14 pH stainless steel (H900 condition), which is high temperature capable. The working section and intermediate plenum were rated to a design pressure of 10 bar, and protected (in the event of full blockage of the deswirl vane ring) by a 400 mm diameter stainless steel rupture disc. This is designed to disintegrate if the pressure in the intermediate plenum exceeds 9 bar. The stiffness of the blisk was such that at 600 K and 10 bar, the maximum deflection of the hub components was predicted to be 0.4 mm, with a minimum safety factor of 3.0 at the peak stress location within the blisk. By using the blisk structurally, it removes the need for a separate support structure for the hub components. The total mass of the module was approximately 750 kg.

Choke Plate Design. An adjustable choke is integrated into the deswirl vane module, rotatable around its axis by a geared hand-wheel with a sealed shaft extending to the outside of the facility. The choke plate has 30 webs (see Fig. 5(b)) which reduce the deswirl vane passage area to a blockage ratio, B , of up to $B=0.5$. A blockage ratio of 0.5 is sufficient to achieve both cruise and MTO operating points at both cold and warm temperature conditions for all the NGVs standards tested in the ECAT facility. Limiting B to a sensible maximum is a conservative design approach that minimizes the chance of overpressure through user error. The web shape (a profiled arrow shape) was designed to give a profile of blockage ratio as a function of deswirl vane pitch (rotation angle) that offered good control. This profile is shown in Fig. 6 (note fine control at low blockage ratio).

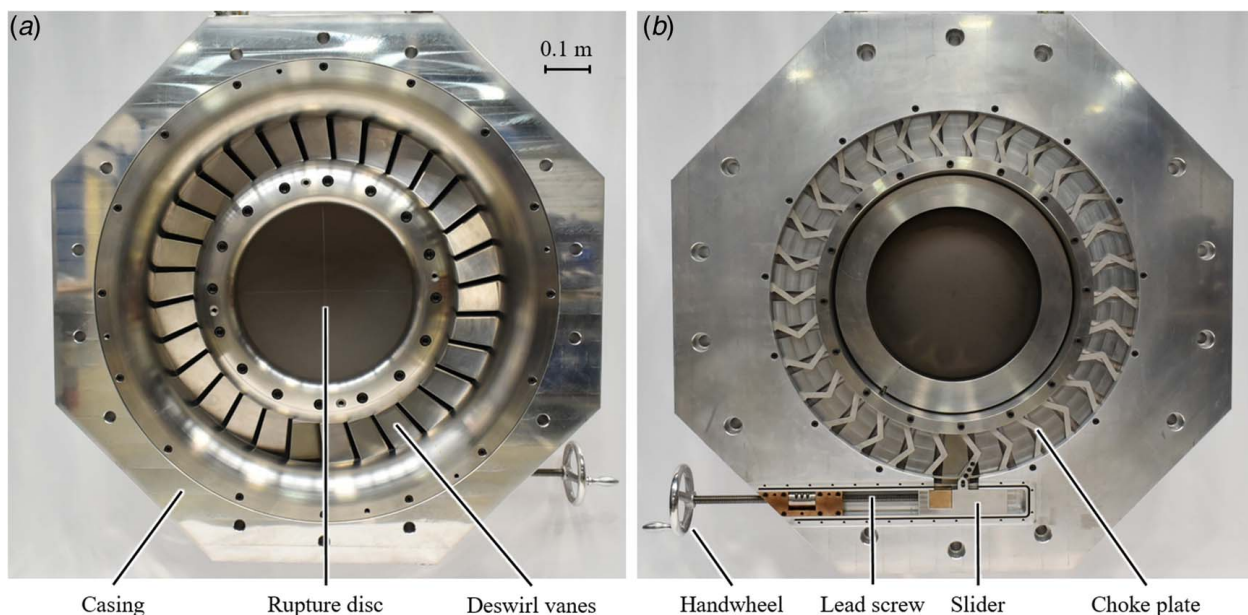


Fig. 5 View of the deswirl module (deswirl vane ring; choke plate; rupture disk) hardware from (a) upstream and (b) downstream

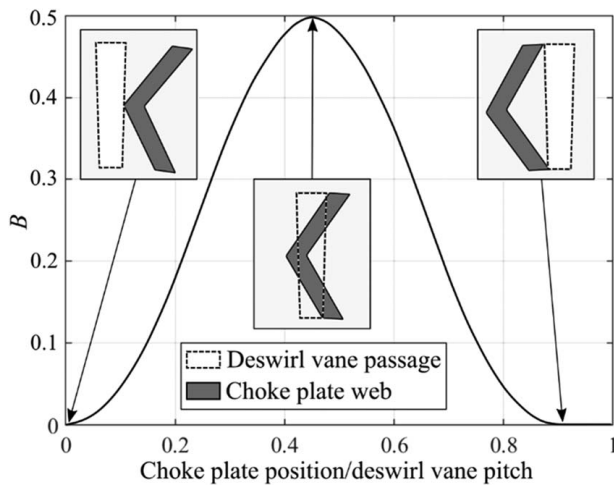


Fig. 6 Choke plate blockage ratio B as a function of plate position normalized by deswirl vane pitch

Experimental Methods

Operational Modes. During the commissioning of the deswirl module, the ECAT facility was operated in two modes: valve-controlled mode and regulated mode. In valve-controlled mode, the mass flowrate is controlled with a butterfly valve at inlet to the flow conditioning and metering pipework for the facility, and a wide range of facility pressure ratios can be achieved in a single run. We define the facility pressure ratio (p_{01}/p_5) as the ratio of total pressure upstream of the NGVs (p_{01}) and the atmospheric pressure in the detuner (p_5). A typical valve-controlled facility pressure ratio characteristic is shown by the dashed line in Fig. 7. The through-flow time (time for complete air exchange in the facility) ranges between 2.5 and 30 ms. This can be taken as proxy for the flow time-constant. In this time, the maximum percentage change in facility pressure ratio is $3.9 \times 10^{-3}\%$. The flow is therefore quasi-steady. This operational mode was used for determining the approximate capacity characteristics for the facility at a range of blockage ratio (positions of the choke plate). Regulated mode can provide true steady operation during 60 s by using a pressure regulator in the pipework. A typical steady facility pressure ratio characteristic of 20 s is shown by the solid line in Fig. 7. This mode was used for aerodynamic measurements and for flow visualization measurements.

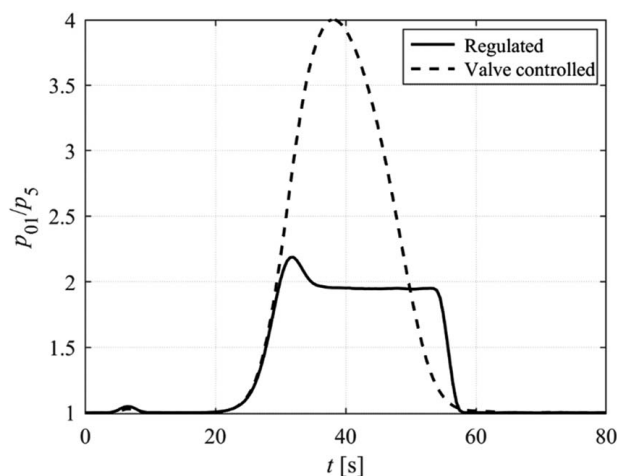


Fig. 7 Typical facility overall pressure ratio characteristics (p_{01}/p_5) during valve-controlled and regulated operation

Instrumentation. To measure the deswirl vane inlet radial total pressure distribution, a radial total pressure rake was installed 0.2 deswirl vane axial chords upstream of the deswirl vanes as shown in Fig. 8.

This rake had 10 beveled-inlet pitot probes oriented at a pitch angle of 0 deg and a yaw angle of 77 deg. The angle was chosen based on the nominal flow whirl angle from CFD. To measure the deswirl vane pressure distribution, an instrumented deswirl vane was installed with 60 static pressure tapings (10 each on SS and PS surfaces at each of 20%, 50%, and 80% span). The instrumented vane was laser sintered in stainless steel with integral internal channels and post-machined to ensure the same surface finish as the non-instrumented vanes. The deswirl vane inlet contraction had eight static pressure tapings on each of the hub and casing walls. The location of all instrumentation is shown in Fig. 1. An uncertainty analysis on all the measured and derived quantities is presented in Appendix B.

Flow Visualization Method. A mixture of clear vegetable oil and fluorescent powder paint was used to visualize the streamlines on the deswirl vanes and the endwalls. The paint mixture was applied with a brush everywhere on five deswirl vanes (red paint), on the hub inlet contraction and passages (green paint), and on the casing inlet contraction and passages (blue paint). The facility was then ran in regulated mode (steady-state) at the nominal facility pressure ratio ($p_{01}/p_5 = 1.974$) with zero blockage ratio for 20 s. Photographs of the streamlines were taken immediately after the run in a dark room under an ultraviolet light.

Numerical Methods

Solver Settings. CFD was used to validate the analytically based preliminary design approach presented earlier. Simulations were performed using ANSYS CFX, with unsteady Reynolds averaged Navier–Stokes (URANS) settings and high resolution discretization (second-order accurate) for both advection and turbulence terms. A second-order discretization scheme was also used for the time derivative. The $k-\omega$ shear stress transport turbulence model with automatic wall functions and the reattachment prediction model were selected. This turbulence model was selected because it blends $k-\epsilon$ and $k-\omega$ models. This is important in our situation because both separated-mainstream and near-wall flows are important. The time-step was based on typical values of the Strouhal number for trailing edge (TE) vortex shedding. According to Sieverding and

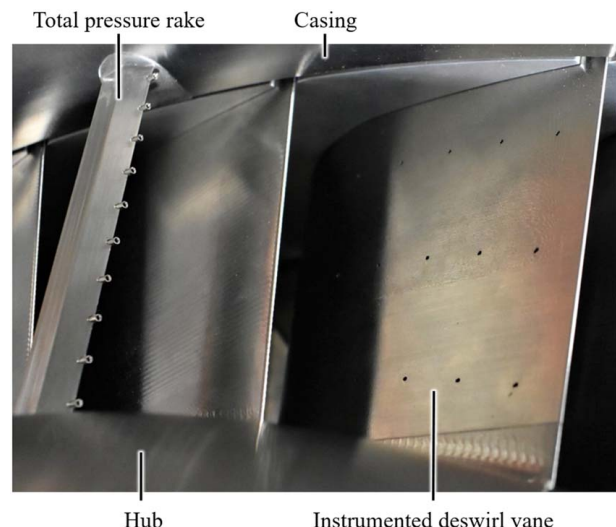


Fig. 8 Upstream total pressure rake and instrumented deswirl vane

Heinemann [29], for turbulent boundary layers on both PS and SS, the Strouhal number (defined by $St = fL/U$, where f is the vortex shedding frequency, U is the mass-averaged velocity at the deswirl vanes exit plane, and L is the TE thickness) is below 0.25. The calculated characteristic vortex shedding frequency f was approximately 3.3 kHz, corresponding to a cycle time period of approximately 3.1×10^{-4} s. A time-step of 10^{-5} s was chosen (approximately 30 time-steps per cycle). Unsteady simulations were initialized with results from a converged steady simulation and run for sufficient time-steps to flush through initial transients. Monitor points in the wake region were used to test convergence of the simulations to a quasi-periodic state. The solution was converged for at least five periods of the velocity signal with the lowest frequency. In this time window, the solution at each mesh node was acquired every 20 time-steps. This corresponds to a sampling time of approximately every 2×10^{-4} s, compared with the dominant periodic time period of 2×10^{-3} s, associated with the time cycle of a large separation in the hub region of the deswirl vane inlet.

Mesh and Boundary Conditions. Meshing was performed using ANSYS ICEM-CFD. The domain included the intermediate plenum (including the NGV exit duct), the deswirl vane, and the detuner. A sector comprising 1/30th of the full annulus was modeled (one deswirl vane passage), and periodic boundary conditions were applied to both sides of the domain. The mesh is shown in Fig. 9. The three subdomains (plenum, deswirl vane, and detuner) were meshed independently with local refinement to enhance mesh quality. The plenum domain was discretized with a fully structured hexahedral mesh, whereas both the deswirl vane and the detuner were meshed using unstructured tetrahedrons. The subdomains were connected via non-conformal general grid interfaces. Grid density was kept high at mesh interfaces to minimize interpolation errors. The overall mesh had approximately 14.7 million hybrid cells (hexahedral and tetrahedral). In the near-wall region, the grid was refined with 15 prism layers with an expansion ratio of 1.2. The value of the non-dimensional wall distance (y^+) was below 10 on most of the wetted surfaces (maximum value below 30).

An inflow boundary condition was imposed at the domain inlet, with specified total pressure, total temperature, flow direction, and turbulence intensity ($Tu = 10\%$). Inlet total pressure and yaw angle were specified as circumferential mass-flux-averaged distributions based on traverse measurement performed at the NGV exit plane, at nominal test conditions (M_2 and Re_2). The measured profiles of total pressure and yaw angle at the NGV exit (domain inlet) are shown in Fig. 10. The mean Mach number during the measurement and yaw angle were $M_2 = 0.97$ and $\beta_2 = 75.8$ deg, respectively. At the domain outlet (detuner), the static pressure was set to atmospheric pressure. A radial equilibrium condition was applied. All wetted surfaces were adiabatic.

It should be noted that changes in facility pressure ratio p_{01}/p_5 in the experiments were achieved by varying the facility inlet total pressure p_{01} for a fixed detuner static pressure p_5 (equal to atmospheric pressure). In CFD, however, the facility pressure ratio was changed by varying the detuner exit static pressure, p_5 (from the nominal atmospheric pressure condition), for a fixed domain inlet total pressure, p_{02} . This strategy was more computationally efficient. Simulations performed in this way are on a single Re_2 - M_2 characteristic, however, and neglect the possibility of Reynolds-dependent loss mechanisms in the dump diffuser. As the flow is dominated by a swirling separated jet, this was taken to be unimportant. We review this assumption later in the paper. The inlet boundary conditions of total pressure and yaw angle are given in Fig. 10. To back-calculate the equivalent facility pressure ratio, p_{01}/p_5 , for the CFD simulations (for comparison with experimental data), the approximate measured value of NGV total pressure loss coefficient $Y_{p,NGV} = 0.05$ (see Eq. (4)) was taken.

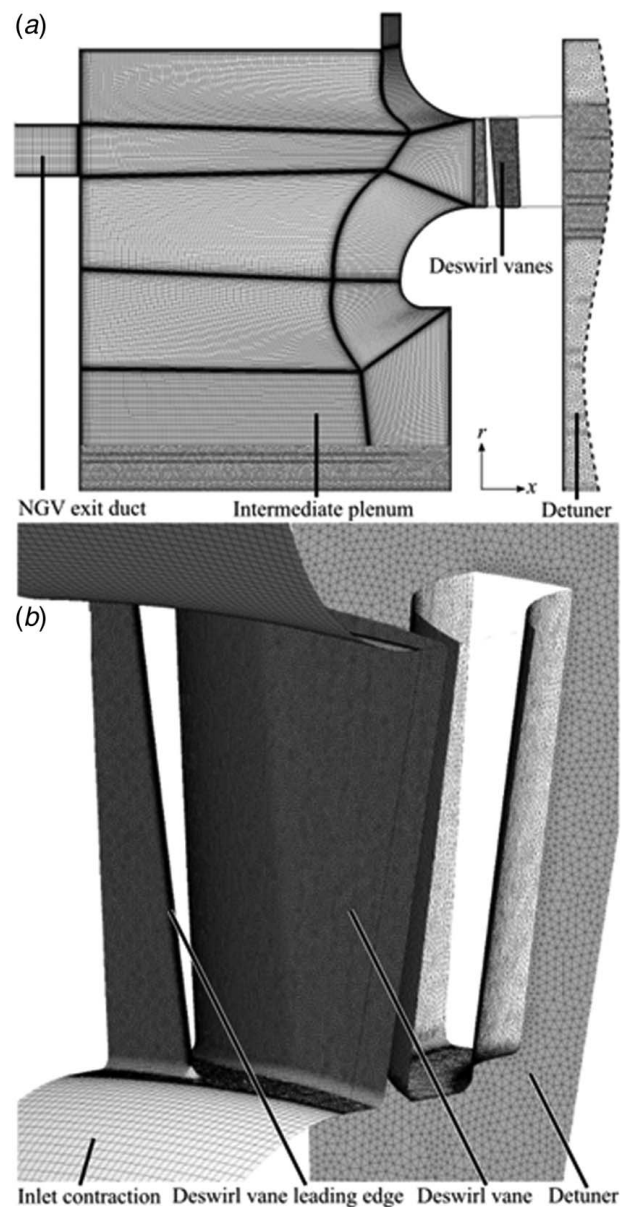


Fig. 9 Computational domain and mesh: (a) cross section and (b) detailed view of the deswirl vane

In all, five simulations were run, with equivalent overall pressure ratios of $p_{01}/p_5 = 1.716, 1.794, 1.974, 2.193,$ and 2.322 .

Analysis of Flow Structure

In this section, we examine the measured and predicted flow properties (pressures, flow angles, and velocities) and streamlines in the HP NGV exit duct, intermediate plenum (dump diffuser), and in the deswirl vane passage to understand the flow structure within the system.

General Description of Flow. Figure 11 shows the predicted time-averaged cross-sectional streamline pattern in the intermediate plenum at the nominal facility pressure ratio ($p_{01}/p_5 = 1.974$) with zero blockage ratio ($B = 0$). The corresponding absolute velocity distribution (we choose this in place of Mach number because of significant total pressure variations) is shown in Fig. 12.

The flow is well behaved (no separation; no significant modification to the radial pressure field) in the short (2.3 NGV axial chords)

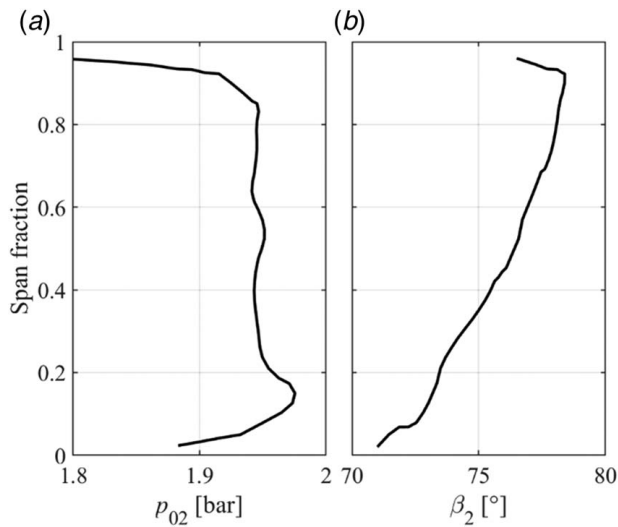


Fig. 10 Spanwise distributions of (a) total pressure and (b) flow yaw angle used as boundary conditions to the CFD domain

parallel exit duct downstream of the HP NGVs. This is important because the deswirl module is designed to control intermediate plenum static pressure without disturbing the radial pressure field at the vane outlet.

In the intermediate plenum, the flow pattern is dominated by a high-velocity central jet (Figs. 11 and 12) with shear layers on either side, driving strong recirculations at both casing and hub. The principal recirculations (driven by the main jet) are marked A and B in Fig. 11; secondary recirculations (driven by the principal recirculations) are marked as C and D. It is recalled that the mean flow yaw angle at domain inlet is $\beta_2 = 75.8$ deg—the recirculations are toroidal in shape with a net recirculation in the whirl direction of the vane.

In the intermediate plenum, the jet is unconstrained and moves to slightly higher radius. This causes a reduction in tangential velocity as a requirement of angular momentum conservation. Friction at the free shear layer also slows the jet. These combined actions explain the slight divergence of the streamlines in the central jet in the downstream direction. This is also clearly observed in the absolute velocity distribution in Fig. 12.

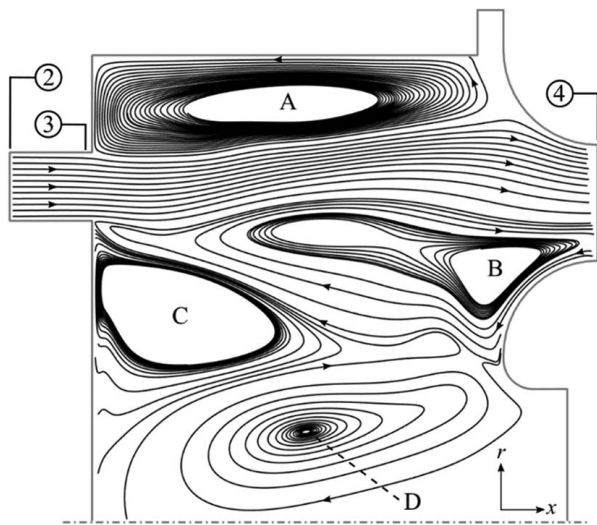


Fig. 11 Predicted time-averaged cross-sectional streamline pattern in the intermediate plenum at nominal pressure ratio and zero blockage ratio

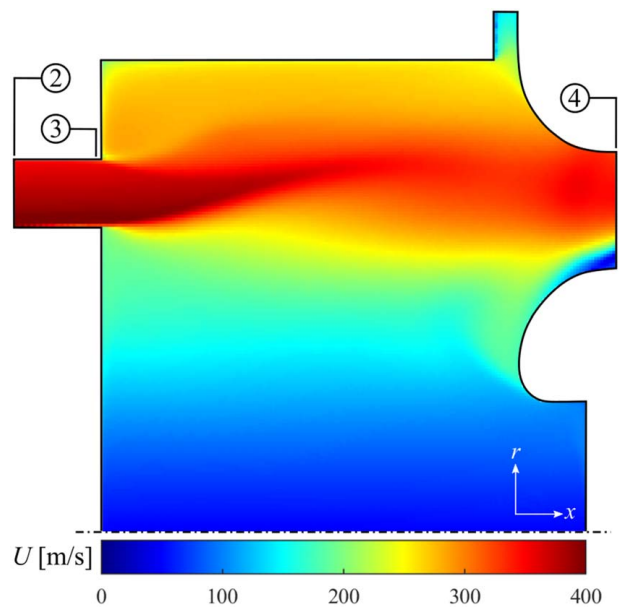


Fig. 12 Predicted time-averaged absolute velocity distribution in the intermediate plenum at nominal pressure ratio and zero blockage ratio

As the flow enters the deswirl module inlet contraction, it is simultaneously forced to lower radius (causing an increase in the tangential velocity) and accelerated (contraction of annulus). As the flow gets deeper into the deswirl vane passage (not shown), the radial pressure field is weakened (reduction of whirl angle), causing a favorable pressure gradient for the casing flow and an adverse pressure gradient at the hub.

It is interesting to note that the recirculation B extends into the deswirl vane passage, with inflow (at the deswirl vanes inlet plane) from the recirculation between approximately 20% and 35% span and outflow between 0% and 20% span. The driving mechanism is as follows: the entire recirculation (between 0% and 35% span at deswirl vanes inlet) is a region of low total pressure inclined to be overturned (towards the hub) by the radial pressure gradient established in the central jet; as the main flow enters the deswirl vane passage the radial pressure gradient is weakened (by taking turning out of the flow), creating an adverse pressure gradient for streamlines in the hub region; the flow between 20% and 30% span is turned down towards the hub, reverses, and flows back out of the passage into hub recirculation B. We examine this effect in greater detail in later sections.

High-Pressure Nozzle Guide Vane Exit Duct Behavior.

Figure 13 shows measured and predicted normalized hub and casing static pressures at the HP NGV exit plane (station 2; see Fig. 1) and at the end of the parallel duct (station 3; see Fig. 1), 2.3 NGV axial chords downstream of the NGV exit plane. Local static pressures are normalized by the upstream total pressure (or implied—via assumed value of $Y_{p,NGV} = 0.05$ —upstream total pressure in the case of the CFD) and plotted as a function of the mean vane isentropic Mach number, $M_{2,is}$. Presented in this way, the radial pressure gradients at the two stations are most apparent (the static pressure profile is approximately linear in the radial direction). In the case of the experiment, the facility pressure ratio was adjusted by varying both the choke plate blockage and the upstream total pressure. The data therefore cover a wide range of Re_2 for a given M_2 . The data across the entire Re_2 – M_2 space overlay very precisely, showing that the ratios p_2/p_{01} and p_3/p_{01} are essentially independent of Re_2 over the range tested. Data without the back-pressure control module are also presented, marked *natural* in the figure. In the CFD data, only the system back-pressure (p_5)

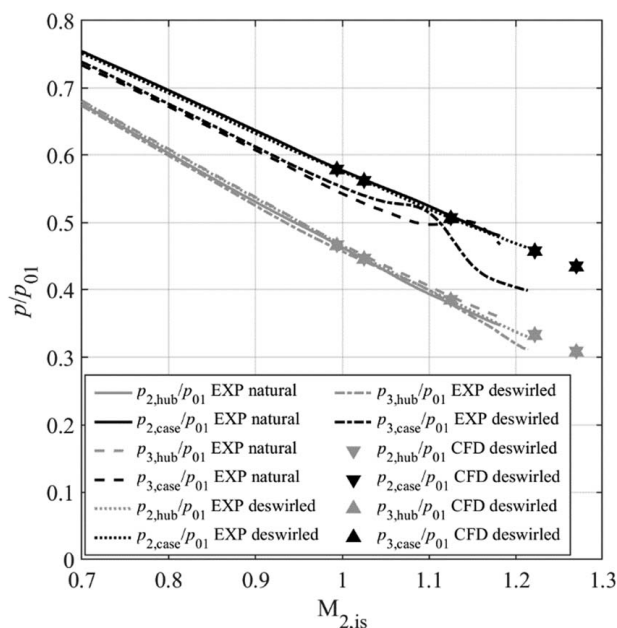


Fig. 13 Measured and predicted normalized static pressures at station 2 (NGV exit plane) and station 3 (duct exit) as a function of NGV mean isentropic exit Mach number

was varied, as a proxy for varying the choke plate blockage, for fixed inlet total pressure. The CFD data are therefore for a single Re_2 - M_2 characteristic in the Re_2 - M_2 space. In the experimental data, p_2 values are the average of 96 tapings each at hub and case, and p_3 values are based on a single tapping. In the CFD data, averages were taken across the entire sector at each location.

Looking first at the experimental data at the NGV exit plane (station 2), we see a well-behaved radial pressure gradient that increases in magnitude with increasing Mach number. The introduction of the back-pressure control module has a negligible effect on the radial pressure gradient in this location, i.e., it appears to be unaffected by the flow structure that develops in the dump diffuser (compared to exhausting directly into the detuner). This confirms that the back-pressure control module does not affect the NGV exit boundary condition. At the same location, the CFD data with deswirl system installed (for $p_{01}/p_5 = 1.716, 1.794, 1.974, 2.193, \text{ and } 2.322$) are in almost identical agreement with the experimental data. This is expected because the inlet boundary of the CFD (imposed boundary conditions from experiment) is very close to station 2.

Looking now at the station 3 data (end of exit duct), we see that in the subsonic range ($0.7 < M_{2,is} < 1.0$) the experimental data show well-behaved radial pressure distributions at all Mach numbers, with slightly lower pressure gradient (relaxation from forced to free vortex, and flow accommodating to relatively constant static pressure condition in plenum) and slightly lower absolute pressure than at station 2. In the transonic range ($1.0 < M_{2,is} < 1.2$), the casing static pressure trend is modified by the introduction of the deswirl system. This effect is almost completely insensitive to deswirl vane blockage (data not shown) and is thought to be caused by a modification of the intensity of the casing vortex (marked A in Fig. 11) due to a global change in secondary flow structure in the dump diffuser (compared with the exhaust duct). The CFD data at station 3 (with deswirl system installed) agree with the station 2 data. That is, unlike the experimental data, there is almost no predicted development (relaxation of radial pressure gradient) of the vortex through the NGV exit duct.

Flow Visualization Results. Experimental flow visualization results are presented in Fig. 14 and compared to predicted surface

streamlines (fourth-order Runge-Kutta path integrals of time-averaged near-wall velocity field). For clarity, companion line drawings of streamline patterns have been recreated for the experimental data by carefully examining the photographs of the parts. We will consider the pressure surface, suction surface, hub, and case walls in turn.

On the PS, the flow is well behaved in both the experiment and CFD. There is moderate downwash of streamlines caused by slight negative pitch angle at the inlet (note the 5 deg downflow of the central jet in Fig. 11), and moderate spreading of streamlines caused by positive incidence at the LE (mean design incidence of 3 deg)—we examine this in more detail later. The experimental and CFD flow patterns are in agreement, with slightly exaggerated downwash in the CFD in the lower forward half of the vane. Both show a hub recirculation region, but the exaggerated downwash in the case of CFD enhances this effect leading to a larger predicted hub recirculation region than seen in the experiment.

Now consider the SS of the vane. The flow pattern is dominated by strong secondary flows, particularly pronounced at the hub, where the cross-passage flow (driven by the extreme cross-passage pressure gradients expected in an impulse-type design) climbs up the SS (marked A) to 50% span at the TE in the case of the experiment, and 70% span in the case of the CFD. Here the flow meets the main flow, and there is a well-defined lift-off line (marked B) marked by counter-rotating vortices (marked C).

On the hub surface (viewed from the gas path to the wall), in both the experiment and the CFD, there is a region of reversed flow in the near-endwall region in the leading part and forward of the deswirl vane. This is the same feature as vortex B in Fig. 11. In the case of the experiment, the reversed flow feature seems to be confined to an extremely small span adjacent to the endwall. Downwash and flow reversal cause the flow on the leading SS of the vane to spill around the PS of the LE into the adjacent passage (marked D). The same feature is apparent in the CFD, but with substantially greater depth in the spanwise (flow reversal up to 20% span; see also Fig. 11) and chordwise directions (reversed flow up to approximately 30% axial chord).

On the casing inlet contraction surface (viewed from the gas path to the wall), the flow is well behaved in both the experiment and CFD. There is mild negative incidence due to the constant LE metal angle (with span) and decreasing flow yaw angle towards the case. This negative incidence angle is more pronounced in the experiment (approximately -4.0 deg) than in CFD (-1.8 deg).

On the casing passage surface (viewed from the gas path to the wall), there is significant over-turning of the low-momentum endwall boundary layer fluid, leading to cross-passage migration of streamlines from the PS to the SS of the vane. This effect is more pronounced in the experiment than predicted, leading to a roll-up into a passage vortex that climbs down on to the SS of the vane at approximately 40% axial chord. By the TE of the deswirl vane, this secondary flow feature extends between approximately 100% and 75% span (marked E). The same features are apparent in the CFD but the point at which the endwall secondary flow climbs down on to the vane surface is less distinct, and the passage vortex fills only the uppermost 15% of the span.

Deswirl System Inlet Conditions. We now consider the inlet conditions to the deswirl vanes. Figure 15 shows the measured and predicted (time-averaged) flow properties at the deswirl vane inlet plane (station 4; see Fig. 1) for the zero blockage ratio case. Results are presented for five overall facility pressure ratios $p_{01}/p_5 = 1.716, 1.794, 1.974, 2.193, \text{ and } 2.322$ with zero blockage.

Figure 15(a) shows the normalized radial total pressure profiles. CFD-predicted pressures were evaluated at the same locations as the pitot probes. Although the NGV outlet flow has relatively constant total pressure (see Fig. 10(a)), the general trend at the deswirl vane inlet is higher at a total pressure towards the casing than the hub. This is broadly consistent with the general flow pattern of Fig. 11, in which there is a separated mixing jet with mass flow

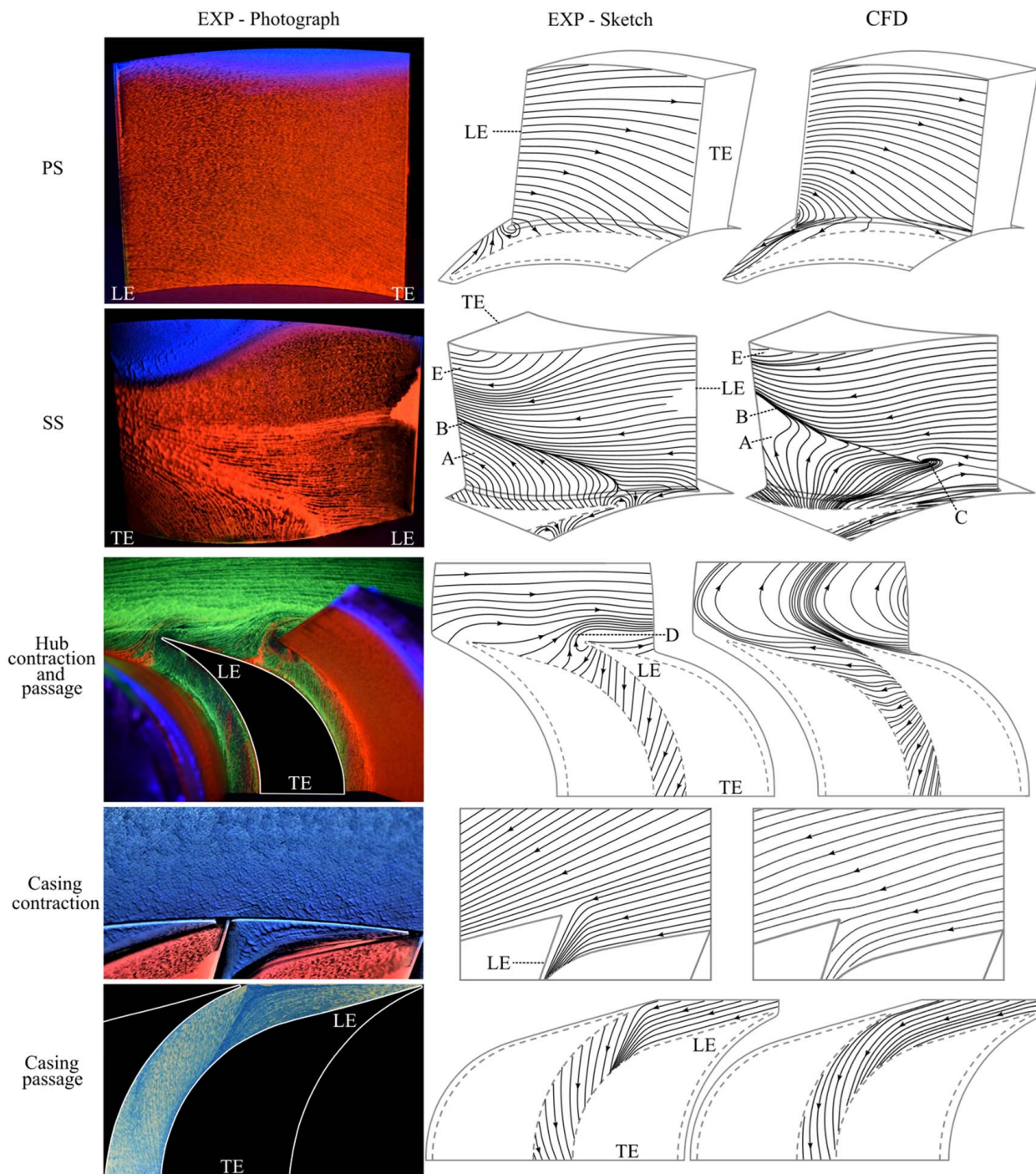


Fig. 14 Comparison of experimental and CFD flow visualization at the nominal pressure ratio and zero blockage ratio

biased towards the casing (representing lower sensitivity to loss in mixing shear layers) and higher absolute velocity (on account of the radial static pressure field) towards the hub (representing greater opportunity for loss). This trend is exaggerated in the CFD compared to the experiment, suggesting that the CFD underpredicts the jet mixing (a common problem with the URANS method) and overpredicts the migration of the jet towards the casing. There is a reduction in normalized total pressure with increasing facility pressure ratio, consistent with higher vane exit Mach number and higher associated absolute loss. In a later section we qualify this loss using a loss coefficient for the dump diffuser.

Figure 15(b) shows the radial profiles of normalized static pressure upstream of the deswirl vanes. The experimental profiles

were measured with the first spanwise row of pressure tappings on the SS of the instrumented deswirl vane (see Fig. 8) and pressure tappings on the hub and casing upstream of the deswirl vanes (see Fig. 1). The incidence angle is non-zero, and therefore the leading SS static pressures are an imperfect proxy for the undisturbed static pressure (i.e., that *upstream* of the deswirl vanes). A small correction is required, and the method is summarized in Appendix A. The measured and predicted profiles have a similar shape, with an approximately linear trend between 100% and 20% span (consistent with highly whirling flow) and approximately constant static pressure below 20% span. For the predicted results, the constant static pressure below 20% span is in agreement with the large separation in this region (see Fig. 11). The CFD departs from the experiment

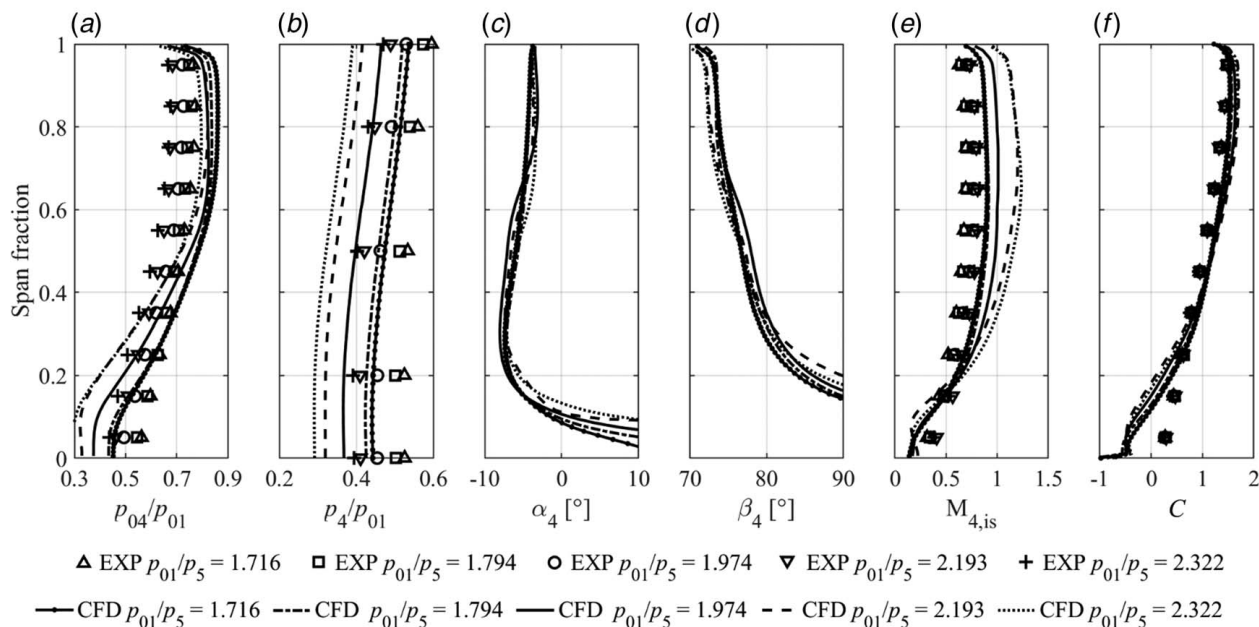


Fig. 15 Measured and predicted (time-averaged) flow properties upstream of the deswirl vanes for different facility pressure ratios and zero blockage ratio: (a) normalized total pressure, (b) normalized static pressure, (c) pitch angle, (d) yaw angle, (e) isentropic Mach number, and (f) normalized mass flux

and in that it significantly underpredicts the mean static pressure at all facility pressure ratios (p_{01}/p_5). Taken in combination with a higher mass-flux-averaged total pressure (or lower dump diffuser loss coefficient), this suggests significantly lower local *effective* area than in the experiment. This could be the result of a higher predicted whirl angle, or a jet that is more constrained in the radial direction.

Figure 15(c) shows the predicted time-averaged radial pitch angle distribution at the location of the rake. The pitch angle is negative (range between -4 deg and -8 deg) between 20% and 100% span, caused by the downward deflection of the primary jet (see Fig. 11). In the hub region (0–20% of the span), the flow is separated, and the predicted pitch angle tends to values close to 180 deg corresponding to reverse flow along the hub wall (see Fig. 11).

Figure 15(d) shows the predicted time-averaged radial yaw angle distribution at the location of the rake. Comparing to Fig. 10(b) (yaw at NGV exit), we see that the mass-flux-averaged yaw angle at the deswirl vane inlet plane is 77.0 deg compared with 75.8 deg at the NGV exit. Interestingly—but not surprisingly—there is a reversal of the gradient of the yaw angle with radius: at the NGV exit, the yaw angle increases with radius (forced vortex created by the NGV), but at the deswirl vane inlet plane the yaw angle decreases with radius (similar trend to free vortex, in which the tangential velocity is proportional to $1/r$). Between the NGV and the deswirl vane, the separated jet *relaxes* from a forced to a free vortex. Below 20% span the flow is separated (large, separated recirculation, marked B in Fig. 11) and reversed.

The pitch and yaw angles are (on the basis of the CFD predictions) relatively independent of the overall facility pressure ratio in the range $1.716 < p_{01}/p_5 < 2.322$, varying by on average ± 0.71 deg between 20% and 100% span. In addition, the pitot probes (pre-pitch of 0 deg and pre-yaw of 77 deg) are within a compound incidence angle of less than 13 deg across the 20–100% span range. As for the hub region (0–20% span), flow visualization has shown that the experimental flow is not reversed on the hub endwall surface. This suggests that incidence angles (both pitch and yaw) with respect to the rake pitot tubes should be below 20 deg in this region. In this range, errors in (uncorrected) total pressure should be less than 1.00% for beveled-inlet pitot probes [30] of the type used.

Figure 15(e) shows the experimentally inferred and predicted isentropic Mach number distributions at the deswirl vane inlet plane ($M_{4,is}$). The experimentally inferred $M_{4,is}$ was calculated using the total and static pressures measured (p_{04}) and inferred (p_4 ; see Appendix A for method) upstream of the deswirl vanes. Looking at the experimental data, we see a relatively constant $M_{4,is}$ between 35% and 95% span, with $M_{4,is}$ increasing with overall facility pressure ratio. At the nominal facility pressure ratio, the mass-flux-averaged $M_{4,is}$ was 0.71. The corresponding value (at same facility pressure ratio) predicted by CFD was 0.84: a moderate overprediction. The overprediction of $M_{4,is}$ is a result of the combined effect of the underprediction of the both the dump diffuser static pressure and the total pressure loss coefficient.

Figure 15(f) shows a distribution of a *normalized mass flux function* upstream of the deswirl vanes: specifically, the local mass flowrate per unit of local geometric passage area ($\dot{m}_{4,l}/A_{4,g,l}$) normalized by the mean value of the same or—equivalently—the ratio of the total mass flowrate and total area ($\dot{m}_4/A_{4,g}$). That is, we define the normalized mass flux function by:

$$C = (\dot{m}_{4,l}/A_{4,g,l})/(\dot{m}_4/A_{4,g}) \quad (5)$$

where the local mass flowrate $\dot{m}_{4,l}$ was calculated from the spanwise distributions static pressure (p_4) and total pressure (p_{04}), and the predicted flow angles (α_4 and β_4 ; values in the 0–20% span region were extrapolated from the rest of the span). This normalized mass flux function has the following properties: it has an average value of unity across the span; values above unity show regions where the local mass flux (i.e., the area-independent mass flowrate) is higher than average; values below unity show the reverse. In a uniform flow, a constant value of unity would be expected and the purpose in the definition is to allow description of deviations from that state.

In both the experimental and CFD data, we see a significantly casing-loaded normalized mass flux function, with average experimental values in the range 1.3–1.5 near the casing and approximately 0.3–0.5 (i.e., a mean ratio of approximately 3.5) near the hub. This is partly explained both by the central jet (Figs. 11 and 12) carrying significantly high total pressure (Fig. 15(a)) in the near-casing region but is also associated with the effective blockage caused both by large-scale separations within the deswirl vane

passage near the hub (0–20% span in the case of CFD) and secondary flows extending between 0% and 50% span. Although both experiment and CFD have similar trends, the CFD trend is exaggerated on account of reversed flow in 20% span region nearest the hub.

We use this description of the flow conditions in the intermediate plenum and upstream of the deswirl vanes to inform analysis of the deswirl vane surface pressure distributions and measured capacity deficit functions.

Dump Diffuser Loss Coefficient. To better understand the total pressure data of Fig. 15(a) and to retrospectively evaluate the assumptions about dump diffuser loss used for capacity setting of the deswirl vane, we now calculate the dump diffuser total pressure loss coefficient ($Y_{p,DD}$) as a function of the NGV isentropic exit Mach number for both the experimental and CFD data.

Taking Eq. (3), \bar{p}_{02} was calculated from p_{01} (measured) using an assumed (from traverse measurements [22]) NGV total pressure loss coefficient ($Y_{p,NGV} = 0.05$). \bar{p}_{04} was calculated by averaging the spanwise distribution of p_{04} weighted by the local mass flowrate ($\dot{m}_{4,l}$) at each span position. The resulting trend of $Y_{p,DD}$ with NGV isentropic exit Mach number, $M_{2,is}$, is presented in Fig. 16 for both experimental and CFD data. The experimental data are presented for both zero and 0.25 choke plate blockage ratio B (representing a range of $1.51 \times 10^6 < Re_2 < 3.48 \times 10^6$ at $M_{2,is} = 0.9$). It is recalled that the CFD simulations were performed for a single Re_2 – M_2 characteristic. The experimental data for $Y_{p,DD}$ are in the range $0.59 < Y_{p,DD} < 0.71$ over a fairly wide range of $M_{2,is}$ and Re_2 . The loss coefficient increases slightly with $M_{2,is}$ for $M_{2,is} > 0.4$ but is relatively insensitive to Re_2 . This justifies the CFD method that was used. The CFD data show lower loss (under-prediction of the jet mixing rate) and less sensitivity to $M_{2,is}$, with all loss coefficients in the range $0.34 < Y_{p,DD} < 0.37$ over a Mach number range $1.00 < M_{2,is} < 1.29$. The preliminary design value of $Y_{p,DD} = 0.5$ appears to have been a reasonable choice for setting the deswirl vane capacity.

Deswirl Vane Pressure Distribution. We now consider the deswirl vane aerodynamics. Figure 17 shows the measured and predicted (time-averaged) isentropic Mach number (M_{is}) distributions at 20%, 50%, and 80% span. Data are presented for the nominal facility pressure ratio, $p_{01}/p_5 = 1.974$, and zero blockage ratio. For the experimental data, M_{is} was calculated using local surface static pressure (Fig. 8) and the span-relevant total pressure measured using the upstream rake. An identical process was used in CFD,

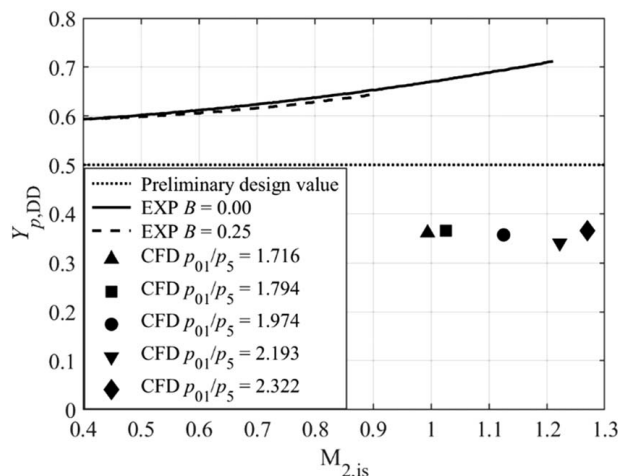


Fig. 16 Measured and predicted dump diffuser mass-flux-averaged total pressure loss coefficient as a function of NGV isentropic exit Mach number based on rake measurements

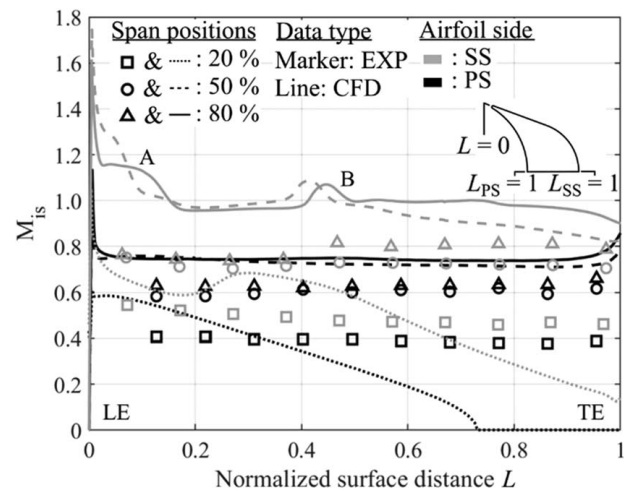


Fig. 17 Measured and predicted distributions of deswirl vane surface isentropic Mach number at the nominal facility pressure ratio and zero blockage ratio ($B = 0$)

with the additional step of time-averaging the unsteady flow at each location.

We first analyze the CFD data. To aid interpretation, we also consider the corresponding time-averaged area-distributions of M_{is} at 50% and 80% span. These are shown in Fig. 18. For the particular operating condition, the flow upstream of the vanes is high-subsonic, with $M_{is} = 0.98$ and $M_{is} = 0.99$ at 50% and 80% span, respectively. This is shown in the radial distributions of $M_{4,is}$ in Fig. 15(e) and in the contour plot of Fig. 18. With respect to the mean LE metal angle, the local incidence angles at 50% and 80% span are 5.4 deg and 2.2 deg, respectively. Taking account of the LE radius, the corresponding local turning angles on the SS of the vane are 3.4 deg and 0.2 deg at 50% and 80% span, respectively, and 7.4 deg and 4.2 deg on the PS. At both 50% and 80% span, we see a local acceleration (caused by positive incidence) round the SS LE tip, leading to a locally supersonic patch (marked A in Figs. 17 and 18) extending between 0% and approximately 15% surface distance. Excluding the LE spike, the peak Mach number in this region is approximately 1.30 at 50% span and 1.15 at 80% span. Beyond this local suction peak, the flow appears to isentropically diffuse back to a Mach number of approximately unity (i.e., close to the inlet Mach number). At approximately 40% surface distance on the SS, there is a local acceleration and diffusion (marked B in Figs. 17 and 18). This is located at the blend point between the flat and curved (constant radius) sections that form the vane SS construction. The pressure disturbance is thought to arise because of the discontinuity in the surface curvature at this point [31]. On the remainder of the SS, there is a relatively constant M_{is} distribution for the 80% span section and a slight reduction in M_{is} with surface distance for the 50% span section. On the PS of the vane, M_{is} has an almost constant value at approximately 0.75. The pressure difference across the passage is therefore relatively constant with surface distance, consistent with constant PS curvature and constant turning rate within the passage (impulse-type vane). The 20% span CFD pressure distribution is primarily within a separated region and is presumably primarily driven by the pressure distribution of the nearby non-separated flow.

Looking now at the experimental data, we observe similar general trends but different absolute magnitude. At the 50% and 80% span sections, the pressure gradient across the passage is similar to the CFD, but with average SS M_{is} of 0.72 and 0.77, respectively. This is consistent with the lower-than-predicted measured Mach numbers in Fig. 15(e). At 20% span the pressure distribution is consistent with attached flow within the passage, but at very low local Mach number or total pressure (see Figs. 15(a)–15(e)). This is also consistent with the flow visualization results (Fig. 14) which show

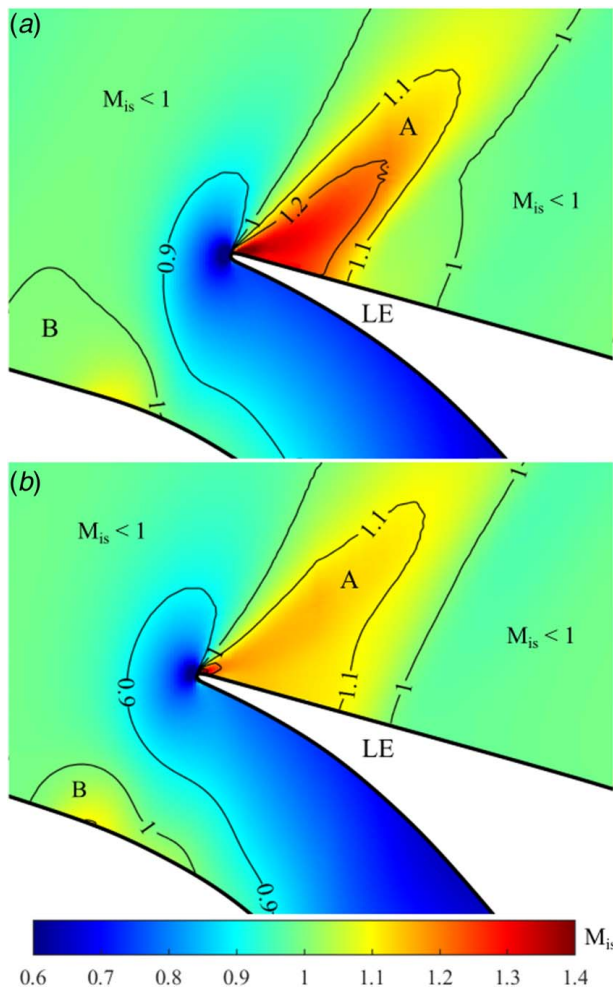


Fig. 18 Time-averaged predicted isentropic Mach number distributions at the leading edge of a deswirl vane at the nominal facility pressure ratio and zero blockage ratio: (a) 50% span and (b) 80% span

only a local reversed flow region near the LE of the vane in the experimental data, but a larger scale reversed flow region in the CFD.

Back-Pressure Control, Total Pressure Loss, and Capacity Relationship

We now consider the performance of the system for the purpose of back-pressure control and attempt to understand the system characteristics by considering the dump diffuser total pressure loss and the deswirl vane capacity.

Back-Pressure Control. In this section, we look at the HP NGV back-pressure as a function of facility pressure ratio using experimental data. Blockage ratio was evaluated geometrically (see Fig. 6).

Figure 19 shows measured span-averaged NGV exit isentropic Mach number characteristics as a function of facility pressure ratio for various blockage ratios. The *natural* (no deswirl module) operating characteristic and the characteristics for 11 blockage ratios are shown. As a discussion example, we consider operation at $M_2 = 1$. Condition A (marked in Fig. 19) is the *natural* operating point with no deswirl module corresponding to the lowest achievable back-pressure in practice. Condition B represents the minimum facility pressure ratio (and associated Re_2) that can be achieved with the deswirl module installed: that is, with a blockage

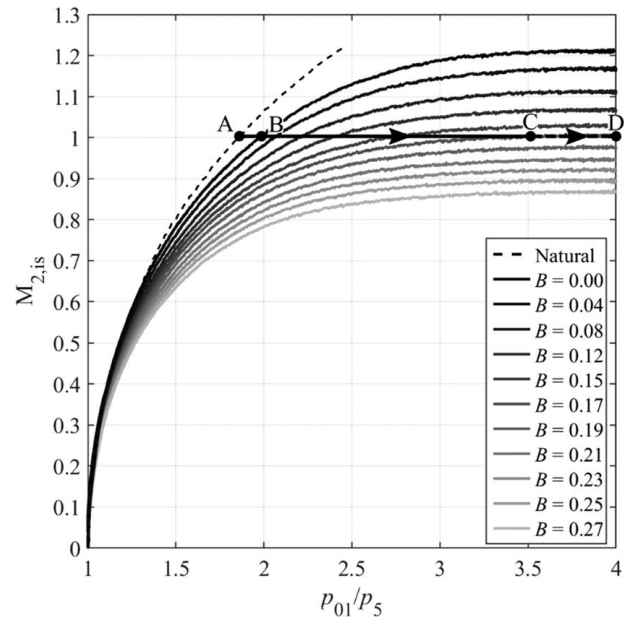


Fig. 19 Experimentally measured HP NGV exit isentropic Mach number characteristics as a function of facility pressure ratio for various blockage ratios

ratio of zero. The minimum back-pressure increases slightly between conditions A and B due to blockage imposed by the deswirl module. Increasing the blockage ratio (moving between B and C) leads to an increase in Re_2 . In this blockage range, the *deswirl vane* mean inlet Mach number increases from high-transonic to choked. In the region between C and D (and beyond), both the NGV and the deswirl vane are choked and indefinite further increases in overall facility pressure ratio (and therefore NGV Re_2) are possible at the same blockage ratio without affecting the NGV exit Mach number.

The overall performance curves for the deswirl module are most compactly represented as M_2-Re_2 characteristics. These are shown in Fig. 20, marking in particular: the natural operating characteristic, eleven characteristics at particular blockage ratios, and the M_2-Re_2 conditions for the five particular CFD simulations. The conclusion is that excellent M_2-Re_2 control can be achieved with good sensitivity over a wide range. The deswirl module works well for the intended purpose providing precise control of operating point.

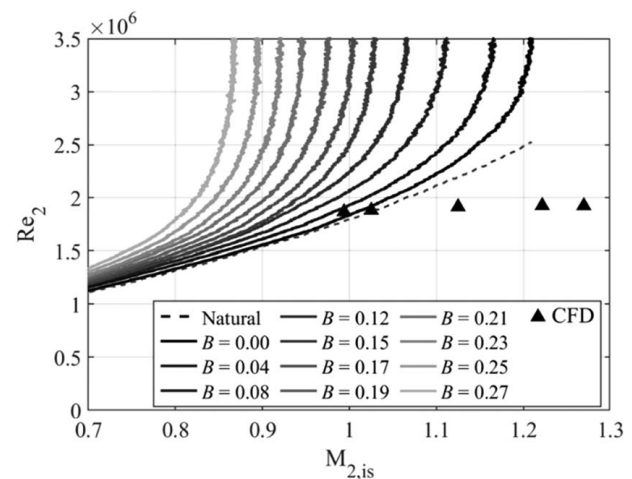


Fig. 20 Experimentally measured M_2-Re_2 relationship for the HP NGVs as a function of blockage ratio. Individual CFD simulations are also marked.

Taking the nominal operating point as $M_{2, is} = 1$, the experimentally measured minimum value of Re_2 was 1.84×10^6 or 1.66% greater than the natural operating point. This compares well with the predicted increase in minimum Reynolds number of 3.32%, partially validating assumptions made in setting the required capacity overhead during preliminary design.

Total Pressure Loss. To understand the deswirl vane capacity deficit (discussed in the next section), we calculate the experimentally evaluated mass-flux-averaged dump diffuser total pressure loss coefficient at every *system operating point* $Y_{p, DD}(p_{01}/p_5, B)$. We present the results in this form—as opposed to the more natural co-ordinate system $Y_{p, DD}(p_{02}/p_2)$ —to allow us to calculate the capacity deficit at every system operating point. $Y_{p, DD}$ was defined according to Eq. (3), using the mass-flux-averaged total pressure upstream of the deswirl vane (calculated by averaging the spanwise distribution of p_{04} weighted by the local mass flowrate $\dot{m}_{4, l}$ at each span position). $Y_{p, DD}$ was measured without traverse equipment and infrared cameras installed in the intermediate plenum, but the additional loss associated with these is expected to be small in comparison to the loss associated with the dump diffuser. The results are presented in Fig. 21.

Over a very wide range of facility pressure ratio ($1.0 < p_{01}/p_5 < 4.0$) and blockage ratio ($0 < B < 0.25$), the total pressure loss coefficient varies in the range $0.59 < Y_{p, DD} < 0.71$: a relatively limited range. The value of $Y_{p, DD} = 0.59$ can be taken as the incompressible limit, with $Y_{p, DD} = 0.71$ corresponding to $M_{2, is} = 1.2$, the highest isentropic Mach number tested. Vertical contours at low values of p_{01}/p_5 indicate a slow increase in the value of $Y_{p, DD}$ with increasing compressibility. Independence of $Y_{p, DD}$ on pressure ratio for high values of p_{01}/p_5 (horizontal contours) occurs when the deswirl vane is choked, setting a particular NGV exit Mach number (both subsonic or mildly supersonic) for a given blockage ratio. In this region, increasing blockage lowers the NGV exit Mach number and lowers the corresponding value of $Y_{p, DD}$. In the next section, we consider the implied capacity deficit based on geometric area.

Deswirl Vane Capacity Deficit. Using the results of Fig. 21 as a representation of \bar{p}_{04} (see Eq. (3)), we can compute the *measured* deswirl vane capacity $\Gamma_4(\bar{p}_{04}/p_5, B)$

$$\Gamma_4(\bar{p}_{04}/p_5, B) = \frac{\dot{m} \sqrt{T_{04}}}{\bar{p}_{04}} \quad (6)$$

We can also define an isentropic geometric capacity function [25] $\Gamma_{4, is}(\bar{p}_{04}/p_5, B)$ using the full geometric passage area, $A_{4, g}$, and the

blockage (see Fig. 6), as

$$\Gamma_{4, is}(\bar{p}_{04}/p_5, B) = (1-B)A_{4, g} \sqrt{\frac{\gamma}{R} \left(\frac{p_5}{\bar{p}_{04}} \right)^{(\gamma+1)/2\gamma}} \left\{ \left[\left(\frac{p_5}{\bar{p}_{04}} \right)^{(1-\gamma)/\gamma} - 1 \right] \frac{2}{\gamma-1} \right\}^{1/2} \quad (7)$$

Noting that the deswirl vane pressure ratio (\bar{p}_{04}/p_5) is uniquely defined by the overall facility pressure ratio (p_{01}/p_5) and the blockage ratio (B)—that is $\bar{p}_{04}/p_5 = f(p_{01}/p_5, B)$ —we can make the co-ordinate transform in Eqs. (6) and (7) between $\Gamma(\bar{p}_{04}/p_5, B)$ and $\Gamma(p_{01}/p_5, B)$. Doing so allows us to define a capacity deficit function $\zeta(p_{01}/p_5, B)$ by

$$\zeta(p_{01}/p_5, B) = \frac{\Gamma_{4, is}(p_{01}/p_5, B) - \Gamma_4(p_{01}/p_5, B)}{\Gamma_{4, is}(p_{01}/p_5, B)} \quad (8)$$

This expresses the *effective blockage* in the deswirl vane due to the combined effects of inlet separation, secondary flow within the vane, shock loss, and the exit vena contracta effect. A plot of $\zeta(\bar{p}_{04}/p_5, B)$ is presented in Fig. 22.

Over the range of facility pressure ratio ($1.0 < p_{01}/p_5 < 4.0$) and blockage ratio ($0 < B < 0.25$), the deswirl vane capacity deficit varies in the range $0.125 < \zeta < 0.180$ —a relatively narrow range—decreasing slightly with increasing p_{01}/p_5 . Over most of this range, ζ is essentially independent of blockage, with only slight dependence for $p_{01}/p_5 > 3.5$.

The conclusion is that the capacity deficit (or effective blockage) due to secondary effects within the deswirl vane is essentially constant (at approximately 0.15) across an extremely wide range of operating conditions of overall facility pressure ratio and choke plate blockage. This makes operation relatively linear and leads to easy preliminary design of future systems. The experimentally determined value of 0.15 justifies the use of the value of 0.2 during the preliminary design phase. It is noteworthy that the capacity deficit of the deswirl vanes is high in comparison to typical HP NGVs, which are typically in the range 0.05–0.1, the lower limit being capped by total pressure loss coefficients ($Y_{p, NGV} \sim 0.05$ for transonic vanes) and the upper end of the range typically only applying for heavily aft-loaded vanes with significant static pressure variation across the controlling region [24]. This is perhaps unsurprising because of the extreme secondary flows within the impulse-turbine-type passage.

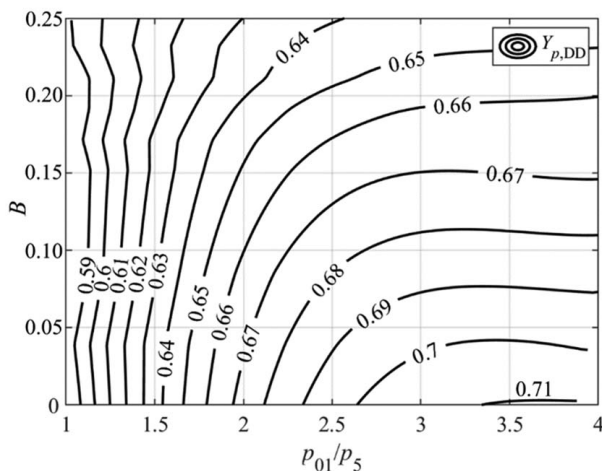


Fig. 21 Experimentally determined dump diffuser mass-flux-averaged total pressure loss coefficient as a function of facility pressure ratio and blockage ratio

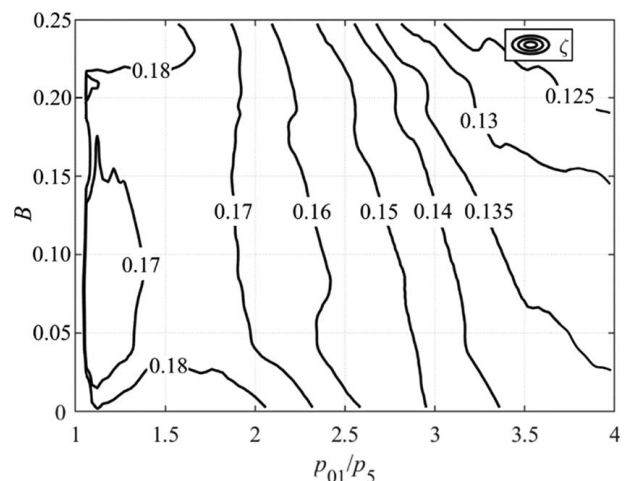


Fig. 22 Capacity deficit function as a function of facility pressure ratio and blockage ratio

Conclusions

In scaled turbomachinery testing, it is often important to have independent control over Mach number and Reynolds number. This is achieved with independent control of the inlet total pressure and exit static pressures in a test facility. In this paper, we present the design and commissioning of a novel back-pressure control system which combines an annular dump diffuser and deswirl system with integrated choke plate. The purpose of the system is to facilitate precise back-pressure control while maintaining access for traverse and optical equipment. The application is in annular cascades in which there is a requirement for independent control of Reynolds and Mach numbers. The new system is uniquely compact, and—by virtue of being manufactured as a blisk—does not require an additional hub support structure. Using experimental and CFD data we perform a comprehensive analysis of the flow that develops in the annular dump diffuser and within the deswirl vane ring.

A preliminary design method is described which will help designers of future systems. This considers both local aerodynamic aspects and overall capacity-loss relationships, leading to a required *capacity overhead* for a specified increase in minimum Reynolds number with the introduction of the system. The proposed low-order design method is recommended for preliminary design because of the ability to predict a wide range of operating conditions with sufficient accuracy for the intended purpose. In the case of the present system, the a priori prediction was for a 3.32% increase in minimum Reynolds numbers: a value of 1.66% was achieved in practice, the slight discrepancy arising because of conservatism in design assumptions. An experimentally determined total pressure loss coefficient for the dump diffuser is calculated, as is the capacity deficit function for the deswirl vane ring (characterizing the impact of secondary flows and loss within the deswirl vane passage), allowing greater precision in preliminary design of future systems.

The new system has a number of installation and control advantages over previous systems, and it is hoped that this analysis will prove useful to designers of future facilities.

Acknowledgment

The financial support of Rolls-Royce plc is gratefully acknowledged. Nafiz Chowdhury is thanked for his support with the experiments.

Conflict of Interest

There are no conflicts of interest.

Data Availability Statement

The authors attest that all data for this study are included in the paper.

Nomenclature

f	= frequency
i	= incidence angle
\dot{m}	= mass flowrate
p	= static pressure
r	= radial position
t	= time
x	= axial position
y^+	= non-dimensional wall distance
A	= area
B	= deswirl vane passage area blockage ratio
C	= normalized mass flux function
L	= characteristic length
M	= Mach number

R	= ideal gas constant
U	= velocity
p_0	= total pressure
\bar{p}_0	= mass-flux-averaged total pressure
T_0	= total temperature
Y_p	= total pressure loss coefficient
Re	= Reynolds number
St	= Strouhal number
Tu	= turbulence intensity

Greeks Symbols

α	= pitch angle
β	= yaw angle
γ	= ratio of specific heat capacities
Γ	= capacity
ζ	= capacity deficit

Subscripts

1	= station 1 (upstream of the HP NGVs)
2	= station 2 (downstream of the HP NGVs)
3	= station 3 (HP NGV exit duct outlet)
4	= station 4 (upstream of the deswirl vanes)
4'	= static pressure tapings at LE SS on deswirl vane
5	= station 5 (downstream of the deswirl vanes)
DD	= dump diffuser
g	= geometric
is	= isentropic
l	= local

Superscript

*	= sonic condition
---	-------------------

Appendix A: Experimentally Inferred Static Pressure Upstream of the Deswirl Vanes

Because the flow incidence angle is non-zero at the deswirl vane LE, the leading SS static pressures (see Fig. 8) are an imperfect representation of the undisturbed upstream static pressure. We now describe the correction method used to recover an inferred value for upstream static pressure. The method is as follows:

- We assume that the flow is subsonic. This is justified by the CFD data at most operating pressure ratios and also by inability to achieve converged solutions in a similar method to the current one in which a supersonic inlet state is assumed (with associated shock/expansion structure on the deswirl vane).
- We assume that the measured static pressure on the SS of the deswirl vane, $p_{4'}$, is equivalent to the upstream static pressure *as disturbed by a subsonic diffusion* around the LE SS of the vane. This is associated with an angle change in the flow equal to the incidence angle, i . This is shown in Fig. 23.
- Referencing the equivalent upstream area, A_4 , and equivalent downstream area, $A_{4'}$, to the equivalent sonic reference area A^* (we take it as the same upstream and downstream because the process is isentropic), we get

$$\frac{A_4}{A^*} = \left(\frac{A_{4'}}{A^*} \right) \left(\frac{\cos(\beta_4)}{\cos(\beta_4 - i)} \right) \quad (A1)$$

Using these area ratios and the area-Mach-number relationships, we calculate the inferred undisturbed upstream static-to-total pressure ratio p_4/p_{04} from the post-diffusion value $p_{4'}/p_{04}$.

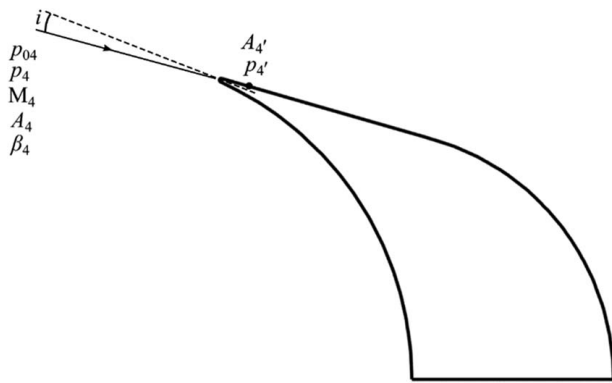


Fig. 23 Schematic of deswirl vane in subsonic flow for calculation of inferred undisturbed upstream static pressure

Appendix B: Bias Uncertainty Analysis

The bias uncertainty in the measured and derived quantities is now considered. All values are quoted to 95% confidence.

The relative bias uncertainty of the NGV inlet total pressure and total temperature ($\sigma_{p_{01}}^{\%}$ and $\sigma_{T_{01}}^{\%}$) were estimated to be $\pm 0.044\%$ and $\pm 0.096\%$, respectively [23]. The relative bias uncertainty of the downstream static pressures ($\sigma_{p_2}^{\%}$ and $\sigma_{p_3}^{\%}$) were estimated to be $\pm 0.019\%$ and $\pm 0.200\%$, respectively [23]. The relative bias uncertainty of the mass flowrate ($\sigma_{\dot{m}}^{\%}$) and NGV capacity ($\sigma_{\Gamma_1}^{\%}$) were estimated to be $\pm 0.531\%$ and $\pm 0.495\%$, respectively [23].

The total pressure upstream of the deswirl vanes (p_{04} , nominal value 1.5 bar) was measured with a rake of 10 internally beveled pitot probes with a relative measurement uncertainty due to installation effects of $\pm 1.00\%$ for flow incidence below 20 deg [30]. The probes are connected to pressure transducers of range 5.0 bar, with quoted bias uncertainty of $\pm 0.04\%$ of full-scale range. The relative measurement bias uncertainty ($\sigma_{p_{04}}^{\%}$) was therefore estimated to be $\pm 0.04(5.0/1.5) \pm 1.00 = \pm 1.133\%$.

Deswirl vane surface static pressures ($p_{\text{deswirl vane}}$, nominal value 1.0 bar) were measured with pressure transducers with range 5 bar and a quoted bias uncertainty of $\pm 0.04\%$ of full-scale range. The relative bias uncertainty ($\sigma_{p_{\text{deswirl vane}}}^{\%}$) was therefore estimated to be $\pm 0.04(5.0/1.0) = 0.200\%$.

The atmospheric pressure in the detuner (p_5 , nominal value 1.0 bar) was measured with a mercury barometer with a quoted uncertainty of ± 1.00 mbar. The bias relative measurement uncertainty ($\sigma_{p_5}^{\%}$) is therefore 0.100%.

The relative bias uncertainties of derived quantities ($\sigma_{M_{2, \text{is}}}^{\%}$, $\sigma_{\text{Re}_2}^{\%}$, $\sigma_{Y_{p, \text{DD}}}^{\%}$ and $\sigma_{\Gamma_4}^{\%}$) were calculated from the bias uncertainties of measured quantities. For any function of a set of entirely independent variables, $F = f(a, b, \dots)$, the relative bias uncertainty in the value of the function can be estimated from the root-sum-squared method

$$\sigma_F^{\%} = \left[\left(\frac{\partial F}{\partial a} \right)^2 \frac{a^2}{F^2} \sigma_a^{\%2} + \left(\frac{\partial F}{\partial b} \right)^2 \frac{b^2}{F^2} \sigma_b^{\%2} + \dots \right]^{1/2} \quad (\text{B1})$$

Table 4 summarizes relative bias uncertainties in measured and derived quantities. Uncertainties are generally low, with the exception of that in p_{04} ($\pm 1.133\%$ to 95% confidence), which is dominated by installation-uncertainty associated with incidence angles on the pitot probes. This, in turn, increases the uncertainty in the dump diffuser total pressure loss coefficient ($Y_{p, \text{DD}}$) and the deswirl vane flow capacity (Γ_4) to $\pm 2.919\%$ and $\pm 1.254\%$, respectively. Given the conservative design approach advocated, with significant capacity overhead at the minimum back-pressure condition, these values are acceptable.

Table 4 Summary of relative bias uncertainty measured and derived quantities

Quantity	$\sigma^{\%}$ (95% confidence)
T_{01}	$\pm 0.096\%$
p_{01}	$\pm 0.044\%$
p_2	$\pm 0.019\%$
p_3	$\pm 0.200\%$
p_{04}	$\pm 1.133\%$
$p_{\text{deswirl vane}}$	$\pm 0.200\%$
p_5	$\pm 0.100\%$
\dot{m}	$\pm 0.531\%$
Γ_1	$\pm 0.495\%$
$M_{2, \text{is}}$	$\pm 0.067\%$
Re_2	$\pm 0.131\%$
$Y_{p, \text{DD}}$	$\pm 2.919\%$
Γ_4	$\pm 1.254\%$

References

- [1] Erhard, J., and Gehrler, A., 2000, "Design and Construction of a Transonic Test-Turbine Facility," Proceedings of the ASME Turbo Expo, Munich, Germany, Paper No. 2000-GT-0480.
- [2] Dominy, R. G., 1988, "The Whittle Laboratory Transonic Annular Cascade Wind Tunnel," Proceedings of the 9th Symposium on Measuring Techniques for Transonic and Supersonic Flow in Cascades and Turbomachines, Oxford, UK, Mar. 21–22, pp. 3.1–3.9.
- [3] Vlasic, E. P., Girgis, S., and Moustapha, S. H., 1996, "The Design and Performance of a High Work Research Turbine," *ASME J. Turbomach.*, **118**(4), pp. 792–799.
- [4] Bernardini, C., Takakura, T., Perez, E., Cameron, J. D., and Morris, S. C., 2019, "Development of a 10 MW Facility for Gas Turbine Engine and Component Testing," AIAA Propulsion and Energy Forum, Indianapolis, IN, Paper No. 2019-4001.
- [5] Wiers, S. H., and Fransson, T. H., 1998, "A New Annular Sector Cascade Test Facility to Investigate Steady State Cooling Effects," Proceedings of the 14th Symposium on Measuring Techniques for Transonic and Supersonic Flow in Cascades and Turbomachines, Limerick, Ireland, Sept. 2–4, pp. 9.1–9.8.
- [6] Rehder, H., Pahs, A., Bittner, M., and Kocian, F., 2017, "Next Generation Turbine Testing at DLR," Proceedings of the ASME Turbo Expo 2017, Charlotte, NC, Paper No. GT2017-64409.
- [7] Kost, F., and Giess, P.-A., 2004, "Experimental Turbine Research at DLR Goettingen," *J. Gas Turbine Soc. Jpn.*, **32**(6), pp. 47–56.
- [8] Hilditch, M. A., Fowler, A., Jones, T. V., Chana, K. S., Oldfield, M. L. G., Ainsworth, R. W., Hogg, S. I., Anderson, S. J., and Smith, G. C., 1994, "Installation of a Turbine Stage in the Pyestock Isentropic Light Piston Facility," Proceedings of the ASME Turbo Expo 1994, The Hague, Netherlands, Paper No. 94-GT-277.
- [9] Povey, T., Chana, K. S., Oldfield, M. L. G., Jones, T. V., and Owen, A. K., 2001, "The Design and Performance of a Transonic Flow Deswirling System," Proceedings of the IMechE Advances of CFD in Fluid Machinery Design Seminar, London, June 13, pp. 1–26.
- [10] Povey, T., Chana, K. S., Jones, T. V., and Oldfield, M. L. G., 2003, "The Design and Performance of a Transonic Flow Deswirling System—An Application of Current CFD Design Techniques Tested Against Model and Full-Scale Experiments," *Advances of CFD in Fluid Machinery Design*, IMechE Professional Engineering Publishing, London, pp. 65–94.
- [11] Povey, T., Jones, T. V., and Oldfield, M. L. G., 2007, "On a Novel Annular Sector Cascade Technique," *ASME J. Turbomach.*, **129**(1), pp. 175–183.
- [12] Ainsworth, R. W., Schultz, D. L., Davies, M. R. D., Forth, C. J. P., Hilditch, M. A., Oldfield, M. L. G., and Sheard, A. G., 1988, "A Transient Flow Facility for the Study of the Thermofluid-Dynamics of a Full Stage Turbine Under Engine Representative Conditions," Proceedings of the ASME 1988 International Gas Turbine and Aeroengine Congress and Exposition, Amsterdam, Netherlands, Paper No. 88-GT-144.
- [13] Sieverding, C. H., and Arts, T., 1992, "The VKI Compression Tube Annular Cascade Facility CT3," Proceedings of the ASME 1992 International Gas Turbine and Aeroengine Congress and Exposition, Cologne, Germany, Paper No. 92-GT-336.
- [14] Epstein, A. H., Guenette, G. R., and Norton, R. J. G., 1984, "The MIT Blowdown Turbine Facility," Proceedings of the ASME 1984 International Gas Turbine Conference and Exhibit, Amsterdam, Netherlands, Paper No. 84-GT-116.
- [15] Dunn, M., and Mathison, R., 2014, "History of Short-Duration Measurement Programs Related to Gas Turbine Heat Transfer, Aerodynamics, and Aeroperformance at Calspan and The Ohio State University," *ASME J. Turbomach.*, **136**(4), p. 041004.
- [16] Paniagua, G., Cuadrado, D., Saavedra, J., Andreoli, V., Meyer, T., Solano, J. P., Herrero, R., Meyer, S., and Lawrence, D., 2018, "Design of the Purdue Experimental Turbine Aerothermal Laboratory for Optical and Surface Aerothermal Measurements," *ASME J. Eng. Gas Turbines Power*, **141**(1), p. 012601.
- [17] Parker, J. A., Romero, E., and Povey, T., 2019, "A Modular Transonic Turbine Cascade for Cooled Rotor Metal Effectiveness Investigations," Proceedings of the ASME Turbo Expo 2019, Phoenix, AZ, Paper No. GT2019-91697.

- [18] Povey, T., Oldfield, M. L. G., and Haselbach, F., 2008, "Transonic Turbine Vane Tests in a New Miniature Cascade Facility," *Proc. Inst. Mech. Eng. Part A*, **222**(5), pp. 529–539.
- [19] Chana, K. S., Singh, U. K., and Povey, T., 2004, "Turbine Heat Transfer and Aerodynamic Measurements and Predictions for a 1.5 Stage Configuration," Proceedings of the ASME Turbo Expo 2004, Vienna, Austria, Paper No. GT2004-53951.
- [20] Beard, P. F., Adams, M. G., Nagawakar, J. R., Stokes, M. R., Wallin, F., Cardwell, D. N., Povey, T., and Chana, K. S., 2019, "The LEMCOTEC 1½ Stage Film-Cooled HP Turbine: Design, Integration and Testing in the Oxford Turbine Research Facility," Proceedings of 13th European Conference on Turbomachinery Fluid Dynamics & Thermodynamics, Lausanne, Switzerland, Apr. 8–12, pp. 1–13.
- [21] Kirollos, B., Lubbock, R., Beard, P., Goenaga, F., Rawlinson, A., Janke, E., and Povey, T., 2017, "ECAT: An Engine Component Aerothermal Facility at the University of Oxford," Proceedings of the ASME Turbo Expo 2017, Charlotte, NC, Paper No. GT2017-64736.
- [22] Burdett, D., and Povey, T., 2022, "Experimental and Numerical Analysis of Loss Characteristics of Cooled Transonic Nozzle Guide Vanes," *ASME J. Turbomach.*, **144**(5), p. 051009.
- [23] Burdett, D., Hambidge, C., and Povey, T., 2020, "Analysis of Ultra-Low Uncertainty Gas Turbine Flow Capacity Measurement Techniques," *Proc. Inst. Mech. Eng. Part A*, **235**(5), pp. 1053–1079.
- [24] Burdett, D., Goenaga, F., and Povey, T., 2021, "Understanding Capacity Sensitivity of Cooled Transonic Nozzle Guide Vanes: A Parametric Experimental and Computational Study of the Impact of Trailing Edge Geometry," *ASME J. Turbomach.*, **143**(5), p. 051001.
- [25] Povey, T., Sharpe, M., and Rawlinson, A., 2011, "Experimental Measurements of Gas Turbine Flow Capacity Using a Novel Transient Technique," *ASME J. Turbomach.*, **133**(1), p. 011005.
- [26] Messenger, A., and Povey, T., 2020, "Calibrated Low-Order Transient Thermal and Flow Models for Robust Test Facility Design," *J. Glob. Power Propuls. Soc.*, **4**, pp. 94–113.
- [27] Luque, S., and Povey, T., 2010, "A Novel Technique for Assessing Turbine Cooling System Performance," *ASME J. Turbomach.*, **133**(3), p. 031013.
- [28] White, F. M., 2009, *Fluid Mechanics*, 7th ed., McGraw-Hill, New-York.
- [29] Sieverding, C. H., and Heinemann, H., 1990, "The Influence of Boundary Layer State on Vortex Shedding From Flat Plates and Turbine Cascades," *ASME J. Turbomach.*, **112**(2), pp. 181–187.
- [30] Gracey, W., Letko, W., and Russell, W. R., 1950, *Wind-Tunnel Investigation of a Number of Total Pressure Tubes at High Angles of Attacks*, National Advisory Committee for Aeronautics, Washington, DC, RM L50G19.
- [31] Korakianitis, T., and Papagiannidis, P., 1993, "Surface-Curvature-Distribution Effects on Turbine-Cascade Performance," *ASME J. Turbomach.*, **115**(2), pp. 334–341.